



Article

The Spread of Multiple Droughts in Different Seasons and Its Dynamic Changes

Shuang Zhu ^{1,2}, Wenying Huang ^{1,2}, Xiangang Luo ^{1,2,*}, Jun Guo ³ and Zhe Yuan ⁴

¹ School of Geography and Information Engineering, China University of Geosciences, Wuhan 430074, China; zhushuang@cug.edu.cn (S.Z.); 1202121937@cug.edu.cn (W.H.)

² Hubei Key Laboratory of Regional Ecology and Environmental Change, School of Geography and Information Engineering, China University of Geosciences, Wuhan 430074, China

³ School of Civil and Hydraulic Engineering, Huazhong University of Science and Technology, Luoyu Road 1037, Wuhan 430074, China; prof_guojun@hust.edu.cn

⁴ Changjiang River Scientific Research Institute, Changjiang Water Resources Commission of the Ministry of Water Resources of China, Wuhan 430010, China; yuanzhe@mail.crsri.cn

* Correspondence: luoxiangang@cug.edu.cn; Tel.: +86-13995523517

Abstract: Investigating the propagation and influencing mechanism that transitions a meteorological drought to a hydrological drought in a changing environment is crucial for understanding the formation process and mechanism of hydrological drought. Furthermore, it is essential to establish an effective hydrological drought warning system based on meteorological drought. To assess the dynamic changes in the spread of meteorological drought to hydrological drought during various seasons, this study employs the Standardized Precipitation Index (SPI), Standardized Runoff Index (SRI), and Normalized Vegetation Index (NDVI) to represent meteorological, hydrological, and vegetation droughts, respectively, in the Ganjiang River Basin (GRB) from 2002 to 2020. Considering that meteorological drought can be caused not only by insufficient precipitation but also by excessive evaporation, an additional index, namely the Evaporative Demand Drought Index (EDDI), is constructed to quantify meteorological drought resulting from evaporation factors. The article analyzes the characteristics of the spatiotemporal evolution of meteorological, hydrological, and vegetation drought. The Spearman rank correlation coefficient is employed to calculate the propagation time of different seasons from meteorological drought to hydrological/vegetation drought and from hydrological drought to vegetation drought. Furthermore, we examine the propagation relationship among meteorological, hydrological, and vegetation drought in the time-frequency domain through cross-wavelet analysis and explore the key factors and physical mechanisms that influence the propagation of drought in various seasons. The result shows: The propagation time from meteorological to hydrological drought (SPI-SRI) is shortest in spring, extended during summer and autumn, and longest in winter. The meteorological drought arising from excessive evapotranspiration in autumn has the most substantial impact on hydrological drought. Vegetation drought and meteorological/hydrological drought exhibit significant intermittent resonance periods in 0~6 months and significant stable resonance periods in 7~15 months.

Keywords: meteorological drought; hydrological drought; agricultural drought; dynamic evolution; drought propagation



Citation: Zhu, S.; Huang, W.; Luo, X.; Guo, J.; Yuan, Z. The Spread of Multiple Droughts in Different Seasons and Its Dynamic Changes. *Remote Sens.* **2023**, *15*, 3848. <https://doi.org/10.3390/rs15153848>

Academic Editors: Marios Anagnostou, John Kalogiros and Jianzhong Lu

Received: 5 June 2023

Revised: 28 July 2023

Accepted: 29 July 2023

Published: 2 August 2023



Copyright: © 2023 by the authors. Licensee MDPI, Basel, Switzerland. This article is an open access article distributed under the terms and conditions of the Creative Commons Attribution (CC BY) license (<https://creativecommons.org/licenses/by/4.0/>).

1. Introduction

Drought is a common and costly natural disaster [1–3] that frequently arises from water shortage and profoundly impacts agriculture, ecosystems, water supply, and the social economy through transmission within the hydrological cycle. In general, there are four typical types of drought [2,4]: hydrological drought, meteorological drought, agricultural drought, and socio-economic drought. These four types of drought are interconnected in terms of water and energy, and the dissemination of water loss signals between different

drought types is known as drought propagation [5–7]. During a drought, the interplay of various portions of the water cycle and the land-atmosphere feedback processes exacerbate the progression of drought [8]. To enhance drought prevention and mitigate its detrimental impacts, it is imperative to conduct comprehensive and extensive research on drought transmission.

The selection of an appropriate drought index is crucial for accurately describing and assessing drought conditions. Numerous drought indicators have been developed and extensively employed to accurately assess the impact of drought [9]. Meteorological drought, primarily influenced by precipitation and evapotranspiration, is typically evaluated by indices such as the Standardized Precipitation Index (SPI; Mc Kee et al., 1993 [10]), the Standardized Precipitation Evapotranspiration Index (SPEI; Vicente-Serrano et al., 2010 [11]) and the Evaporative Demand Drought Index (EDDI; Hobbins et al., 2016 [12]). SPI is extensively employed as a precipitation-based drought indicator to evaluate drought characteristics such as the severity of drought. While easy for computation and capable of capturing drought variations across various temporal scales [13,14], SPI does not consider the influential role of temperature, a crucial climatic factor. With the gradual warming of the global climate, surface temperatures rise abnormally, accelerating water evaporation [15,16]. Consequently, evaporation demand becomes a factor that cannot be ignored for drought assessment. Therefore, Vicente Serrano et al. expanded the consideration of Potential Evapotranspiration (PET) by incorporating it alongside precipitation in their proposition of SPEI. The responsiveness of SPEI to fluctuations in evaporation demand, as well as its multiscale properties, has made it a widely utilized tool in contemporary drought research [17,18]. Nevertheless, research has demonstrated that the impact of evaporation demand on SPEI is considerably smaller compared to precipitation among the climate variables influencing SPEI [19]. Following that, Hobbins et al. introduced EDDI, which exclusively relies on evaporation demand. EDDI is a drought index with a physical basis, encompassing multiple scales and displaying efficient capability in identifying both abrupt and prolonged droughts [12,20]. In comparison to SPEI and SPI, EDDI demonstrates a higher capacity to capture drought events of greater intensity and longer duration [19]. It also serves as a valuable tool for early warning for agricultural drought, hydrological drought, and fire weather risks. Yao et al. have recently examined the applicability of EDDI in China and reported positive findings [21]. However, there remains a scarcity of studies that utilize EDDI for drought assessment and analysis in China. Hydrological drought often occurs after meteorological drought [22], resulting in a significant reduction in surface water and groundwater reserves due to insufficient supply of water resources. It can be characterized and quantified by standardized indices based on different hydrological variables, including runoff, groundwater level, lake level, etc. Runoff holds particular significance in the hydrological cycle and is of primary concern to water managers. Its ease of observation and simulation makes it the most frequently studied hydrological variable [23,24]. Shukla and Wood developed a multiscale Standardized Runoff Index (SRI) based on simulated runoff, which is designed to identify runoff deficits [25]. This index directly describes the impact of climate anomalies on current hydrological conditions controlled by surface physical processes. Persistent meteorological and hydrological drought will result in inadequate water supply for the necessary soil moisture required for crop growth. This is further compounded by continuous crop transpiration leading to water loss, ultimately resulting in agricultural drought [26,27]. The drought index based on in-situ measurements is currently the most commonly utilized effective method to assess the severity of agricultural drought. The Palmer Drought Severity Index (PDSI), proposed by Palmer [28], is the most typical one. It is capable of effectively simulating the entire process of drought occurrence, development and conclusion. However, this indicator demands substantial data and involves a cumbersome calculation process [29]. It is precisely because of the dependence on on-site data that the spatial coverage of drought indices becomes limited in regions with sparse sampling points. With the maturity and widespread application of remote sensing technology in drought monitoring, this has been

effectively improved [30]. The Normalized Difference Vegetation Index (NDVI) [31] is a frequently utilized remote sensing index primarily employed in the monitoring of agricultural/vegetation drought [32,33]. NDVI offers the advantage of monitoring long-term changes in vegetation vitality. Studies have demonstrated its effectiveness in indicating the severity of vegetation stress caused by water shortage [34].

Scholars have conducted pioneering research on drought propagation based on the theoretical basis of water balance and energy balance in the water cycle, mostly focusing on the spread of meteorological drought to hydrological [35–37]/agricultural drought [3,38,39]. These studies summarized two methods for quantitative study of drought propagation: hydrological modeling and statistical analysis. At regional and global scales, large-scale hydrological and meteorological models have been constructed to capture drought characteristics, reproduce drought propagation characteristics, and successfully simulate general propagation processes between different types of droughts [40–43]. Hydrological modeling approaches are also employed for assessing and quantifying the influence of physical and climatic factors on drought spread. Drought propagation is closely related to climatic factors, including but not limited to climate type, seasonality, and precipitation time [44–46]. The physical factors present in the geographic area, including cover type, topography and hydrological conditions, will also affect the drought propagation mechanism [47]. However, the accuracy of simulation results based on a hydrological model may be affected by the uncertainty of model parameters and imperfect model structure. On the other hand, data-based statistical analysis methods, such as correlation analysis, response function analysis, and machine learning, are extensively employed to investigate the connection and synchronicity between various types of droughts [1]. Correlation analysis focuses on the description of drought propagation by analyzing the response relationship among different types of droughts. The correlation coefficient method is predominantly used in correlation analysis as an effective means to unveil the propagation of dry and wet signals. Studies have shown that the propagation time between different droughts in different climatic regions of China has obvious seasonal patterns [48]. It has been revealed that in the majority of regions within the Yangtze River Basin, the tightest relationship was observed between meteorological and hydrological drought, followed by the relationship between meteorological and agricultural drought [49,50].

Wavelet-based correlation analysis has become increasingly popular for studying drought propagation, surpassing the limitations of the correlation coefficient method regarding the periodicity of propagation time. Researchers have employed various techniques, including cross-wavelet analysis, wavelet coherence, and wavelet cross-correlation, to investigate drought propagation mechanisms in different basins throughout China. The findings have consistently indicated that the transmission time from meteorological drought to hydrological drought is evidently seasonal, as well as hydrological droughts are significantly positively correlated with meteorological drought on different periodic scales [36,51]. Li et al. supplemented agricultural drought and used cross-wavelet analysis to quantify the time-lag relationship of different droughts in the Yangtze River Basin, but their seasonal studies were not involved [52]. The response function method plays a crucial role in statistically examining drought propagation. It emphasizes providing statistical relationships between droughts by considering the attributes of different drought types, encompassing functions such as linear functions [53], nonlinear regression functions [54] and probability functions [55]. Researchers have employed probability function-based models, such as copula methods, to explore the dependencies between different types of drought features and the thresholds that trigger drought propagation [37,55]. Although the seasonality of drought propagation has been confirmed in many studies, variations in precipitation and evapotranspiration across different seasons will have a certain impact on the seasonal propagation time of drought, necessitating further study and quantification.

The propagation time of drought is a significant characteristic of its spread. Currently, extensive research has been conducted on various driving factors affecting drought propagation time. Huang et al. discovered that the El Niño Southern and Arctic Oscillations are

strongly correlated with actual evaporation and have a greater impact on the propagation time from meteorological droughts to hydrological droughts [51]. Van et al. suggested that the connection between meteorological and hydrological droughts may be highly influenced by watershed and local climatic characteristics [42]. Li et al. determined that high-potential evapotranspiration expedites the spread of meteorological drought to agricultural drought, while adequate soil moisture provides relief [56]. Xu et al. stated that anthropogenic activities, including agricultural activities, domestic water supply, and urban expansion, can affect the spread time from meteorological to hydrological droughts [57]. Wu et al. believed that modifications in land utilization and coverage, particularly variations in forest or pasture areas, would have an impact on drought spread [58]. These studies highlight the significant influence exerted by meteorological factors, underlying surface conditions, and human activities on drought propagation time. However, these studies mainly examine drought propagation time on an annual scale. The propagation time between droughts varies across different seasons, with corresponding variations in influencing factors. Current research on drought propagation lacks investigation into seasonal variations and fails to reveal the dynamic characteristics of drought spread in different seasons under changing environmental conditions.

This field primarily focuses on the spread of meteorological drought to hydrological or agricultural drought, with limited research on the complete chain of drought propagation. Furthermore, there are several areas that require improvement. For instance, there has been insufficient investigation of drought propagation between seasons, as most studies concentrate solely on the annual scale. Although the temporal relationship between droughts has been extensively explored, minimal consideration has been given to potential spatial connections. Moreover, given the rapid increase in global surface temperature, it is crucial to recognize that precipitation alone does not fully encompass the essence of drought. When studying the propagation of drought, it is imperative to acknowledge the critical role of evapotranspiration, which links the water, energy, and carbon cycles in terrestrial ecosystems.

This study focuses on investigating the spread of meteorological, hydrological and agricultural droughts across various seasons. It explores the dynamic characteristics of these droughts and conducts quantitative analysis to identify the factors influencing drought propagation. This research will contribute to our understanding of the formation process and mechanism of drought, ultimately enhancing the accuracy of hydrological and agricultural drought forecasting. In a changing environment, studying the dynamics of drought propagation and analyzing changes in the regional water cycle pose significant challenges. If the water cycle accelerates, it indicates a higher frequency of meteorological drought disasters, resulting in shorter response times for drought emergencies and a greater need for establishing an accurate early warning system for droughts.

2. Materials and Methods

2.1. Study Area

The Ganjiang River (Figure 1) serves as a significant tributary of the Yangtze River, spanning a total length of 766 km and encompassing a drainage area of 83,500 square kilometers. The GRB possesses abundant water resources, with surface water amounting to 70.289 billion cubic meters and groundwater reserves of 18.84 billion cubic meters. Over the years (1956–2000), the average total water resources remain at approximately 68.7 billion cubic meters. The area of agricultural land in the GRB accounts for 90.4%, while construction land accounts for 4.5%, and unused land accounts for 5%. Among the agricultural land, forestry land covers 5.514 million square hectares, representing 71.5% of the agricultural land area and 64.7% of the regional land area. The GRB spans across four latitudes, and the natural fall of the main stream is 937 m, resulting in significant climate variations between the northern and southern regions. These differences are mainly manifested in:

1. Temperature

The annual average temperature difference between the northern and southern regions is approximately 3 °C, with the average temperature in the basin being 17.8 °C. The northern region generally experiences higher temperatures.

2. Precipitation

It is noteworthy that the middle reaches of the GRB constitute the low-precipitation region within the basin. The average annual precipitation is merely 1413.2 mm, which is 247.7 mm below the basin average. The lowest precipitation during the rainy season (April to June) occurs in the middle part of the basin, reaching 619.9 mm, which is 403.7 mm lower than the maximum recorded precipitation.

3. Solar Radiation and Sunshine Hours

In the upstream area, solar radiation and sunshine hours are generally high, making it one of the areas with high values in the entire basin. Additionally, the eastern area of the middle and lower reaches experiences higher levels of solar radiation and sunshine hours compared to the western region.

4. Ecological Environment

The environmental conditions within the GRB are generally conducive to ecological well-being, with higher forest coverage compared to the average level in the Poyang Lake Basin. However, certain issues exist regarding forest quality and structural imbalances. The stand structure is unreasonable, with a high proportion of coniferous forest and a small proportion of broad-leaved forest. The distribution of forest ages is characterized by an unbalanced structure, predominantly consisting of young and middle-aged forests with a lower percentage of mature and over-mature forests. Additionally, there are concerns regarding low forest canopy density, low-standing timber volume, and inadequate forest protection function. The issue of soil and water loss remains significant in the GRB, with the upper reaches accounting for 22% of the affected area, the middle reaches 16.7%, and the lower reaches 21.6%. Although soil and water conservation measures in the middle reaches are effective, it is prone to drought, making it a high-frequency drought region.

2.2. Data Description

2.2.1. Digital Elevation Model (DEM) Data

The required DEM data for this research was acquired from the geospatial data cloud (<http://www.gscloud.cn/>, accessed on 2 March 2022), with a spatial resolution of 30 m × 30 m. Initially, the original data are obtained through online calculation. Subsequently, the DEM data for the study area was extracted using the cutting–embedding–reprojection steps techniques based on the boundaries of the GRB. DEM serves as one of the fundamental data requirements for constructing the Soil and Water Assessment Tool (SWAT) model. SWAT is a semi-distributed hydrological model based on process and physical principles, which is well-suited for long-term simulation of hydrological and related processes. Utilizing the DEM data, the SWAT model is capable of employing moisture analysis tools to set reasonable thresholds to perform river network extraction, sub-basin division and slope analysis of the watershed. In this study, the precipitation, evapotranspiration, and runoff data used for calculating the drought index, as well as the NDVI data, are obtained for each sub-basin delineated by the SWAT model.

2.2.2. Land Use Data

Historical land use data (2005 and 2015) utilized in the study is sourced from the Resource and Environmental Science Data Center of the Chinese Academy of Sciences (<http://www.resdc.cn>, accessed on 2 March 2022), generated through manual visual interpretation of Landsat8 remote sensing images. The resolution is 1 km × 1 km. According to the land use classification method, land use types can be classified into six first-level classifications of cultivated land, forest land, grassland, water area, residential land, and

unused land, as well as 25 second-level classifications. The first-level types are mainly divided based on land resources and their utilization attributes, while the second-level types are mainly divided based on the natural attributes of land resources. In order to conform to the land use type classification standard of the SWAT model, the collected land use type data (in secondary form) needs to undergo reclassification using the ArcGIS reclassification function. This reclassification assigns the land use types to their corresponding first-level categories and generates the appropriate SWAT land use type codes. This process ensures that the land use types can be properly recognized by the SWAT model. The land use type map after reclassification is shown in Figure 2.

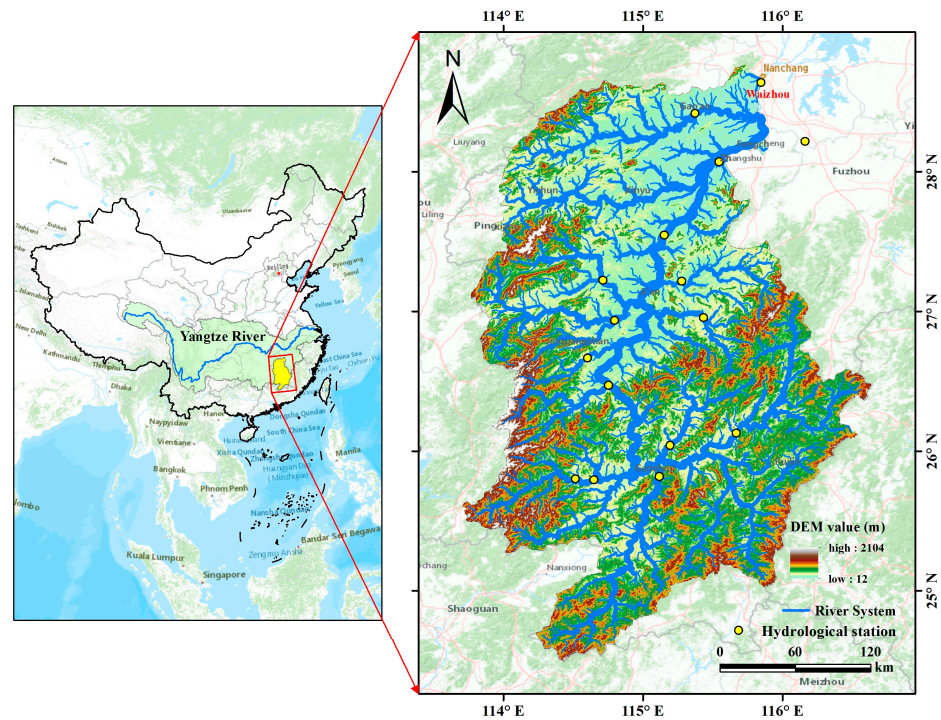


Figure 1. Location map of Ganjiang River Basin. The left figure represents the position of the Ganjiang River Basin in China and the Yangtze River Basin, and the right figure represents the distribution of water systems and hydrological stations in the Ganjiang River Basin.

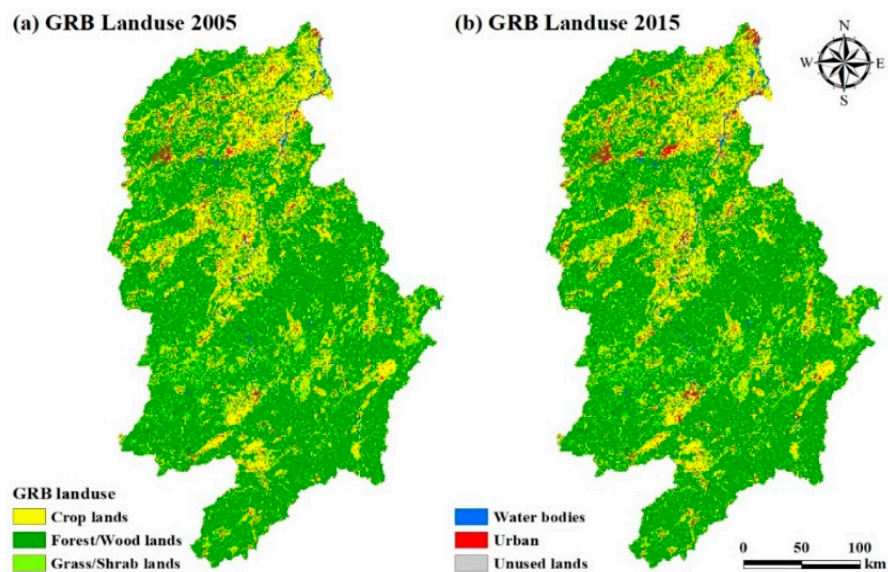


Figure 2. Land use type map of Ganjiang River Basin.

2.2.3. Soil Data

The soil data used in this study comes from the World Soil Database (HWSD) with a spatial resolution of 30 m × 30 m. Soil, as a crucial component of the watershed's underlying surface, significantly influences the runoff and infiltration processes in the hydrological cycle. Therefore, the accuracy of the simulated outcomes of the model are heavily reliant on the precision of each soil type parameter. The soil data in the GRB provided by the HWSD include soil spatial data and a soil attribute database.

2.2.4. Precipitation Data

The precipitation data for this research was derived from the China meteorological forcing dataset (CMFD). The CMFD is a reanalysis dataset of near-surface meteorological and environmental conditions offered by the Institute of Tibetan Plateau Research at the Chinese Academy of Science [59]. The dataset is formatted in NETCDF, with a temporal resolution of 3 h and 1 month, a horizontal spatial resolution of 0.1°, and a time span covering the years between 1979 to 2018. In this paper, the 3 h CMFD is mainly used for runoff simulation, and the monthly CMFD can be used to calculate the meteorological drought index. Since the applicability and reliability of CMFD have been verified in many experiments [60], this dataset has found extensive applications in hydrometeorological forecasting and hydrological investigations [61]. The precision level of this dataset ranges between the observational data of the Meteorological Bureau and the satellite remote sensing data, surpassing the accuracy of the reanalyzed data already available in the world.

2.2.5. Evapotranspiration Data

Evapotranspiration (ET) refers to the process of water entering the atmosphere from the surface [62]. It includes both surface soil evaporation and plant transpiration and plays a crucial role in the energy and water exchange of the soil-vegetation-atmosphere system. In this study, Penman–Monteith–Leuning Version 2 (PML_V2) model was utilized to simulate ET data. The simplicity of its estimation structure does not compromise on reasonable biophysical significance. Furthermore, PML_V2 only necessitates daily meteorological and remote sensing forcing data, making it suitable for regional and global applications [63]. The accuracy and performance of this product surpass that of ground observation data and most existing ET products on a global scale [64,65]. While focusing on the regional scale, PML_V2 still has room for improvement. For example, PML_V2 uses MODIS and GLDAS data as input data to simulate ET. However, as a result of insufficient ground-based observation data in China, the accuracy and applicability of GLDAS data in China need to be improved [66]. This study replaces GLDAS data with CMFD to enhance the accuracy of regional simulation outcomes in China. The produced ET data has a time resolution of 8 days and a horizontal spatial resolution of 500 m, covering the years between 2002 and 2020.

2.2.6. Runoff Data

The rainfall and evaporation data obtained by remote sensing are evenly distributed in space. This type of data provides detailed descriptions of the spatial and temporal characteristics of regional drought. Runoff data is crucial for measuring hydrological drought. However, runoff data is typically only available at flow stations located in river channels, while other areas lack such data. Remote sensing is limited in capturing more precise runoff data. In order to study the spatial characteristics of hydrological drought and correlate it with evaporation and precipitation data, this study employs the SWAT model for simulating spatially distributed runoff data. The model has demonstrated good performance in simulating runoff in the Yangtze River Basin [67]. The data driving the hydrological model includes daily rainfall and monthly runoff data from the GRB Exit Control Station Waizhou Station (28.63°N, 115.84°E). The monthly runoff covers the period from 2002 to 2020. The coefficient of determination (R²) was used to evaluate the applicability of the model.

2.2.7. NDVI Data

The NDVI data utilized in this research is obtained from the MOD13Q1 remote sensing satellite dataset, which originates from the National Aeronautics and Space Administration (NASA) EOS/MODIS data product (<https://modis.gsfc.nasa.gov/>, accessed on 23 April 2022), with a spatial resolution of $250\text{ m} \times 250\text{ m}$ and a temporal resolution of 16 d. This product effectively reflects the vitality and growth status of vegetation and is commonly employed for long-term monitoring of vegetation coverage. In this paper, MODIS Reprojection Tool (MRT) is used to transform and reproject the remote sensing data, and the NDVI data of the GRB area is obtained by batch clipping with ArcPython programming. The NDVI data may exhibit fluctuations due to the complex terrain and weather factors in the GRB. To obtain noise-free and smooth NDVI data, we apply the SG filtering method (Savitzky–Golay Filter) [68]. Subsequently, we perform batch removal of negative values and vector boundary clipping in ENVI software. In the study, the 16-day NDVI was synthesized into monthly NDVI data, and finally, the NDVI image data of 2002–2020 with a spatial resolution of 250 m and a time resolution of a month was obtained.

2.3. Methods

The technical flow chart provides an overview of the main ideas of this study (Figure 3). SPI and EDDI were employed to identify meteorological drought caused by insufficient rainfall and excessive evapotranspiration, respectively. SRI based on simulated runoff and NDVI were used to characterize hydrological drought and vegetation drought. To capture the progression and characteristics of drought development, a three-dimensional spatiotemporal clustering method was employed to extract meteorological and hydrological drought events and their corresponding characteristics based on SPI3, nEDDI3 and SRI3. In order to examine the relationship between different types of drought, the Spearman rank correlation coefficients of SPI_n and SRIn, nEDDI_n and SRIn, SPI_n/nEDDI_n/SRIn and NDVI (where n represents the time scale) were calculated. Afterward, the maximum correlation coefficient (MCC) between different drought types was determined to obtain the propagation times. Based on the MCC, we selected the SPI/nEDDI-SRI and SPI/nEDDI/SRI-NDVI time series with corresponding scales for conducting cross-wavelet and wavelet correlation analysis. This allowed us to assess the propagation relationship among various droughts within the time-frequency realm.

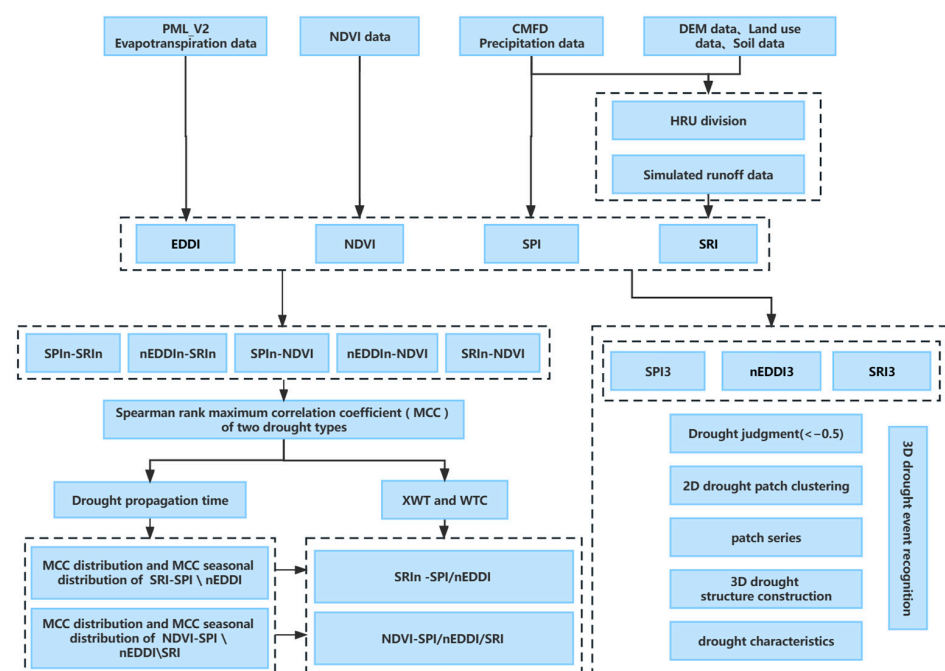


Figure 3. The technical flow chart of this study.

2.3.1. HRU and Runoff Simulation

The SWAT model, developed by the Agricultural Research Center of the United States Department of Agriculture [69], has a robust physical foundation that makes it suitable for complex watersheds with diverse soil types and land types. The model is segregated into the land surface hydrological process and the water surface process. The land surface hydrological process consists of eight modules: hydrology, climate, sediment, soil temperature, crop growth, nutrients and agricultural chemicals. The SWAT model is widely used in runoff simulation, soil erosion simulation, non-point source pollution simulation, transpiration and evaporation simulation [70]. It is compatible with the ArcGIS software, which enhances data processing efficiency, parameter adjustment, and analysis and interpretation of results in the model [71]. The hydrological response unit (HRU) is the basic unit of SWAT model calculation. It divides the basin into several sub-basins with multiple slopes, land use types and soil types. Each sub-basin is further divided into HRUs. Each HRU has a set of parameters to describe its hydrological characteristics and operates independently with no mutual influence. In this study, we defined a HRU of less than 600 km² as a small basin.

The construction and operation of the SWAT model involve the following steps: loading DEM data, extracting river network, sub-watershed division, loading land use and soil type data, dividing HRU, inputting meteorological data, inputting model data file, and operating model. Meteorological data should have a temporal resolution equal to or less than daily, and in this study, we obtained the data from the CMFD with a temporal resolution of 3 h. The hydrological model includes the daily rainfall and monthly runoff data from Waizhou Station, the export control station of the GRB.

2.3.2. Drought Index

In this study, the characterization of meteorological drought resulting from insufficient precipitation is accomplished using SPI. The SPI calculation is based on the principle of converting rainfall data into a normal distribution using the Gamma probability distribution [72]. The specific SPI solution computer program can be obtained on the website of the National Drought Mitigation Center (<http://drought.unl.edu/>, accessed on 5 April 2022).

SPI's remarkable flexibility and multiscale feature make it a versatile tool for quantitative research of different types of drought. SPI with a time scale of 1–3 months effectively captures the short-term and medium-term water status [73]. Specifically, selecting the growing season of vegetation and the seasonal period of crops contributes to a better understanding of agricultural drought. The longer time scale SPI provides insights into meteorological drought over a relatively long period and reveals the prolonged impact of drought events on water resources, considering precipitation variations. SPI with a time scale of 6–24 months can reflect changes in groundwater levels [74], while the 12-month SPI is commonly used for monitoring long-term runoff, reservoirs, and groundwater levels. In this study, the 1, 3, 6, and 12-month SPIs were calculated for 172 sub-basins in the GRB, enabling further exploration of the response relationships between multi-time scale SPI and other indexes in the region.

The characterization of meteorological drought resulting from the atmosphere's excessive water demand was accomplished in this study by employing EDDI. EDDI is a drought index that uses E0 as its foundation, created in response to the recent surge of attention towards evapotranspiration [12]. EDDI has undergone evaluations in multiple regions for its application in drought monitoring [20,21].

After calculating the appropriate probability distribution for each of the 12-time series configured on a monthly basis, the cumulative probability value is transformed through the utilization of the probability distribution of each time series. Subsequently, the converted cumulative probability value is ascribed a Z-value based on the standard normal distribution, representing SPI\EDDI.

The calculation formula of SPI and EDDI at different scales is:

$$f(x) = \frac{1}{\alpha^\beta \Gamma(\beta)} x^{\beta-1} e^{-(x/\alpha)} \quad (1)$$

where x represents the moving average of monthly precipitation or E0 time series on the timescale, α and β represent the scale parameter and shape parameter, respectively, which are estimated by the probability weighted moment method for each time scale and each pixel. $\Gamma(\beta)$ represents a gamma function. SPI and EDDI, obtained via the same method, exhibit opposing drought conditions, with SPI indicating severity through negative values, while EDDI denotes intensity using positive values. To enable a direct comparison between these indices, this study employs negative EDDI (nEDDI) during actual analysis by attaching (-) sign to EDDI.

This study utilizes SRI to characterize hydrological drought, which is a widely used multiscalar drought index in hydrological drought monitoring. We choose the same Γ distribution as SPI to calculate the SRI. The SPI, nEDDI and SRI time series on the 1, 3, 6 and 12-month time scale from 2002 to 2020 were calculated. According to the classification of meteorological droughts based on Nalbantis and Tsakiris [75], SPI, nEDDI and SRI are divided into five grades, and the corresponding thresholds are determined. The levels are shown in Table 1.

Table 1. Drought severity classification in China.

Drought Category	SPI Value	nEDDI Value	SRI Value	Probability (%)
Wet	SPI > -0.50	nEDDI > -0.50	SRI > -0.50	50.0
Mild drought	-1.00 < SPI ≤ -0.50	-1.00 < nEDDI ≤ -0.50	-1.00 < SRI ≤ -0.50	34.1
Moderate drought	-1.50 < SPI ≤ -1.00	-1.50 < nEDDI ≤ -1.00	-1.50 < SRI ≤ -1.00	9.2
Severe drought	-2.00 < SPI ≤ -1.50	-2.00 < nEDDI ≤ -1.50	-2.00 < SRI ≤ -1.50	4.4
Extreme drought	SPI ≤ -2.00	nEDDI ≤ -2.00	SRI ≤ -2.00	2.3

2.3.3. NDVI

This study employed NDVI to characterize vegetation drought. The vegetation growing season in the GRB spans from March to October, during which the imbalance between potential evaporation and precipitation often results in drought, impacting the growth of vegetation. Given the sensitivity of the growing season to drought, our analysis focused on NDVI from March to October each year to examine the spatial-temporal features of vegetation in the GRB and its response to meteorological and hydrological drought.

2.3.4. Identification and Characterization of 3D Drought Events

Drought events typically exhibit certain durations and scopes of influence, displaying the characteristics of being multi-factor, multi-attribute and multiscale in nature. Additionally, various factors, multiple attributes and spatial-temporal scales are interconnected, collectively shaping the spatial-temporal variation characteristics of drought event development processes. This study employed the method proposed by Wen et al. [76] to extract drought events, construct three-dimensional(time, longitude and latitude) drought structures and simulate the evolution process of drought. The identified 3D drought event requires its drought state to be connected in both time and space dimensions. Initially, for each month, sub-watersheds with SPI/nEDDI/SRI values below the specified threshold (-0.5 in this study) were identified as being in a drought state. Spatial clustering is applied to group adjacent drought sub-watersheds in the same month into 2D spatial drought patches. If the drought patches from adjacent months spatially overlap, they are sequentially connected in series to form a 3D drought event. Finally, based on the multi-dimensional grid data sequence (including latitude and longitude, time and drought index), the point data are meshed and interpolated by the inverse distance weighting (IDW) method to generate a continuous spacetime field. The threshold isosurface of the drought

index is then created, and the 3D structure of the drought body is constructed to visualize all three-dimensional drought events.

Then, five parameters are calculated to characterize the identified drought events. Their definitions are as follows:

- Drought duration (DD) is characterized as the period between the onset and cessation of a drought event, measured in months.
- A drought area (DA) can be described as the area that has been impacted by a drought event, defined as the union of affected areas per month.

$$DA = area(1) \cup \dots \cup area(i) \cup \dots \cup area(n) \quad (2)$$

In the formula, n denotes the duration of drought events, and $area(i)$ denotes the drought area determined in the month of i .

- Drought severity (DS) measures the intensity of drought events, which reflects the cumulative absolute deviation between the drought index and the normal state threshold T (-0.5) in the sub-watershed involved in the entire drought duration. It is expressed as:

$$DS = \sum_{i=1}^n \sum_{j=1}^k |DI_{ij} - T| \quad (3)$$

where k represents the number of sub-basins affected by drought, DI_{ij} represents the drought index value of the i th month ($i = 1, 2, \dots, n$) and the j th drought sub-basin ($j = 1, 2, \dots, k$) in the drought event, and the drought index value is SPI\|nEDDI\|SRI value.

- Drought density ($D\rho$) is given by the proportion of drought intensity to the multiplication of drought duration and area to measure the density of drought events.

$$D\rho = \frac{DS}{DD * DA} \quad (4)$$

- Drought centroid (DC) is utilized to denote the center location of the 2D drought patch during the drought event. The centroid coordinates are determined by the weighted drought index value and are expressed as follows:

$$X_m = \frac{\sum_{i=1}^k DI_{mi} x_i}{\sum_{i=1}^k DI_i} \quad (5)$$

$$Y_m = \frac{\sum_{i=1}^k DI_{mi} y_i}{\sum_{i=1}^k DI_i} \quad (6)$$

where (x_i, y_i) represents the latitude and longitude coordinates of the centroid of the i th drought-affected sub-watershed, and DI_{mi} represents the drought index of the i th drought affected sub-watershed in m months.

In light of the aforementioned drought characteristics, this study employs Mann–Kendall (M-K) trend test and weighted kernel density estimation method to analyze its spatial and temporal evolution characteristics. The M-K trend test, a non-parametric statistical method widely used in environmental and climate change research [77–79], provides a reliable approach for assessing trends in time series data. In this study, the M-K trend test is employed to analyze the annual variation trends of drought characteristics. Regarding the statistical value Z , which serves as the measurement index of the trend test, if Z is greater than 0, it indicates an increasing trend, whereas if it is less than 0, it suggests a decreasing trend. The significance test is considered passed when the absolute value of Z exceeds the thresholds of 1.64, 1.96, and 2.58, corresponding to confidence levels of 0.1, 0.05, and 0.01, respectively. The Kernel Density Estimation (KDE) is a non-parametric method [80]. This method examines the distribution characteristics of data based on the data sample itself and is widely employed in regional difference analysis [81,82]. Hence, it is suitable for studying the probability density of the drought centroid. To accomplish this, a fourth-order

kernel function is selected as the kernel function, and the standard distance is weighted, taking into account the area attribute of the drought patch.

2.3.5. Analysis of Drought Propagation Relationship

Cross-Wavelet Transform (XWT) was developed by Hudgins et al. [83] as a useful technique to explore the joint statistical characteristics and correlation between two time series in time-frequency domain. XWT identifies the region of high common power region and phase relationship between the two signals, but it is limited in determining the low common power region. In response, wavelet coherence (WTC) has addressed this limitation and is widely utilized to examine the consistency between two sequences. In the field of meteorology and hydrology, the utilization of Spearman rank correlation coefficient (R_s) is common in measuring the correlation between two variables, whether they are linear or non-linear [54,84].

In this study, SPI- n , nEDDI- n , SRI- n ($n = 1, 3, 6, 12$) and NDVI were used to calculate the drought propagation time between meteorological, hydrological and vegetation droughts based on the Spearman rank correlation coefficient method. Taking SPI and SRI as examples, the R_s can be calculated as follows:

$$R_s = \frac{cov(r_{g_{SRI_i}}, r_{g_{SPI_j}})}{\sigma_{r_{g_{SRI_i}}} \sigma_{r_{g_{SPI_j}}}}, 1 \leq i, j \leq n \quad (7)$$

SRI_i and SPI_j are time series of SRI at a time scale for i months and SPI at a time scale for j months, respectively. $cov(r_{g_{SRI_i}}, r_{g_{SPI_j}})$ is the covariance of rank variables, $\sigma_{r_{g_{SRI_i}}}$ and $\sigma_{r_{g_{SPI_j}}}$ are the standard deviation of rank variables. The time scale of SPI with the MCC will be regarded as the drought propagation time. The p -value of the statistic is calculated based on the permutation test method. When the p -value is less than 0.1, the null hypothesis can be rejected, indicating a significant difference or relationship.

This study investigated the phase shift and correlation among SPI, nEDDI, SRI, and NDVI time series in both high and low-frequency resonance regions using the XWT and WTC techniques. The cross wavelet transform operation involves two time series, x_n and y_n , can be represented as $W^{xy} = W^x W^{y*}$, where $*$ denotes the complex conjugate. This operation yields the corresponding cross-wavelet power spectrum, expressed as $|W^{XY}|$. Notably, the complex parameter $\arg(W^{XY})$ provides valuable information regarding the local relative phase of x_n and y_n . The theoretical distribution of the cross-wavelet power and its background power spectrum P_k^X and P_k^Y [85] are expressed as the following relation:

$$D\left(\left(\frac{|W_n^X(s)W_n^Y(s)|}{\sigma_X\sigma_Y}\right) < P\right) = \left(\frac{Z_v(p)}{v}\right)\sqrt{P_k^X P_k^Y} \quad (8)$$

In the formula, σ_X and σ_Y are the standard deviation of X and Y , respectively. The level of confidence for probability p is represented by $Z_v(p)$, where v denotes the degree of freedom.

The coherence degree of the wavelet transforms between two time series x_n and y_n , can be expressed as:

$$R_n^2(s) = \frac{|S(s^{-1}W_n^{XY}(s))|^2}{S(s^{-1}|W_n^X(s)|^2) * S(s^{-1}|W_n^Y(s)|^2)} \quad (9)$$

where S is a smooth operator. The range of $R_n^2(s)$ value is from 0 to 1, with a value of 0 indicating no local cross-correlation and a value of 1 indicating a strong correlation between the two sequences.

The lag time of two time series is represented by phase difference, which is quantified by wavelet phase angle:

$$a_m = \arg(X, Y) = \arg \left[\sum_{i=1}^n \cos(a_i), \sum_{i=1}^n \sin(a_i) \right] \quad (10)$$

where a_m is the phase relationship of time series X and Y in time-frequency space, and the unit is radian, which can be further quantified according to time scale and periodic scale.

In this study, cross-wavelet transform and wavelet coherence analysis are carried out using the MATLAB toolbox developed by Grinsted et al. [86].

3. Results

3.1. Evaluation of Small Basin Scale Runoff

Following the division of the GRB into 172 sub-watersheds using the slope runoff simulation algorithm, ET and runoff in each sub-watershed were simulated using the PML_V2 and SWAT models, respectively. The accuracy of runoff and ET simulation was then verified and evaluated. To validate the runoff simulation, the simulation results from Waizhou station were fitted to the measured monthly runoff data during the parameter calibration period. The fitting accuracy was evaluated by calculating the R2 between the simulated and measured values, which was found to be 0.88. The overall fitting accuracy suggests the reliability of the runoff simulation results.

3.2. Spatial-Temporal Distribution of Three-Dimensional Drought Events

The meteorological and hydrological drought events in the GRB from 2002 to 2020 were extracted from the SPI3, nEDDI3, and SRI3 values from the long time series, respectively. The spatial-temporal distribution of the 3D drought structure, along with the start and end dates of the drought events, is illustrated in Figure 4. The number of identified precipitation-deficient meteorological drought events, evapotranspiration meteorological drought events, and hydrological drought events were 20, 20, and 15, respectively. In Figure 4a, severe and extreme drought events occurred frequently from 2002 to 2010. The drought events that started in January 2003, November 2007, and July 2010 were the most severe, extensive, and prolonged. From 2011 to 2020, the occurrence of extreme drought events increased, although most drought events were of short-term and medium-term nature with scattered spatial and temporal distribution. The most severe drought events were recorded in February 2013 and February 2019. Figure 4b depicts two extreme droughts during the period from 2002 to 2010, occurring in November 2002 and June 2006, respectively. In comparison to the drought events identified by SPI3 in the same period, the intensity of drought events identified by nEDDI3 was relatively lower, and the temporal distribution of drought events was more scattered. After 2010, the frequency of drought disasters increased. Specifically, three extreme droughts were observed in March 2013, February 2018, and March 2019. In Figure 4c, extreme drought events occurred frequently from 2002 to 2010, with medium and long-term droughts being the prevalent types and longer intervals between droughts. After 2010, there was an increase in the occurrence rate of drought events, but the overall intensity of droughts decreased. Throughout this period, extreme drought events only occurred in April 2017. The most severe droughts were registered in June 2003, December 2006, July 2010, March 2013, and April 2017. These findings concur with previous studies [87–89].

In terms of drought frequency, meteorological droughts occurred more frequently than hydrological droughts. However, the situation is reversed when considering the average duration and severity. Multiple meteorological drought events may continue to impact the same hydrological drought, resulting in an increase in its duration, severity and spatial extent.

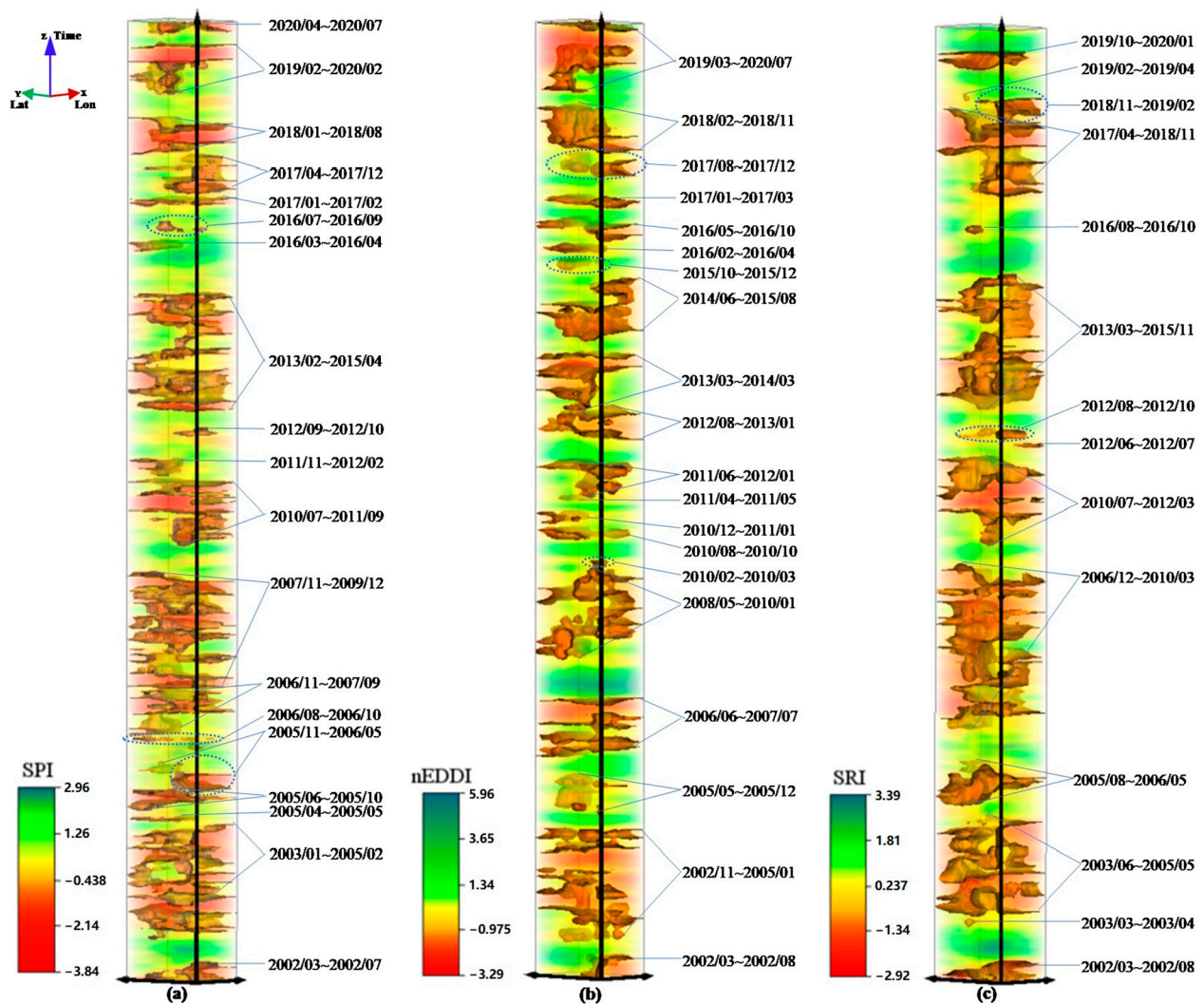


Figure 4. Spatial and temporal distribution of the three-dimensional drought structure of meteorological and hydrological drought events in the GRB from 2002 to 2020. (a) SPI3, (b) nEDDI3, (c) SRI3. The x-axis represents longitude, the y-axis represents latitude, and the z-axis represents time.

3.3. Spatial-Temporal Characteristics of Drought Events

The temporal variation and trends of drought characteristics extracted from meteorological and hydrological drought events in the GRB from 2002 to 2020 are depicted in Figure 5. And the spatial distribution of drought centroids is shown in Figure 6. For meteorological drought events identified by SPI3, the past 19 years have witnessed a downward trend in both the number of drought months and coverage area. Conversely, the drought severity and density showed an increasing trend, indicating an intensification of drought conditions in the basin despite the decrease in overall drought volume. Additionally, the drought events identified by nEDDI3 demonstrate a declining trend in the number of drought months, while other indicators exhibit an upward trend. This suggests a potential development of the drought model towards shorter-term, larger-scale and higher-intensity conditions. The longitude and latitude of the drought centroid exhibited opposite trends, with the longitude decreasing and the latitude increasing. The statistical significance of both trends was confirmed through the M-K analysis at a 95% confidence level. This suggests a potential movement of the drought towards the northwest of the basin, indicating an increased likelihood of more frequent drought events in the northwest region. In regards to the hydrological droughts identified through SRI3, a decreasing trend is observed in the number of drought months, extent, and severity. However, there is a gradual and

consistent increase in drought density. This finding indicates a decrease in the overall volume of hydrological drought events in the GRB, with no significant alteration in the drought intensity. Notably, there is a substantial reduction in the latitude of the drought centroid, implying a potential southward migration of hydrological droughts, which may result in an increased frequency of drought events in the southern region.

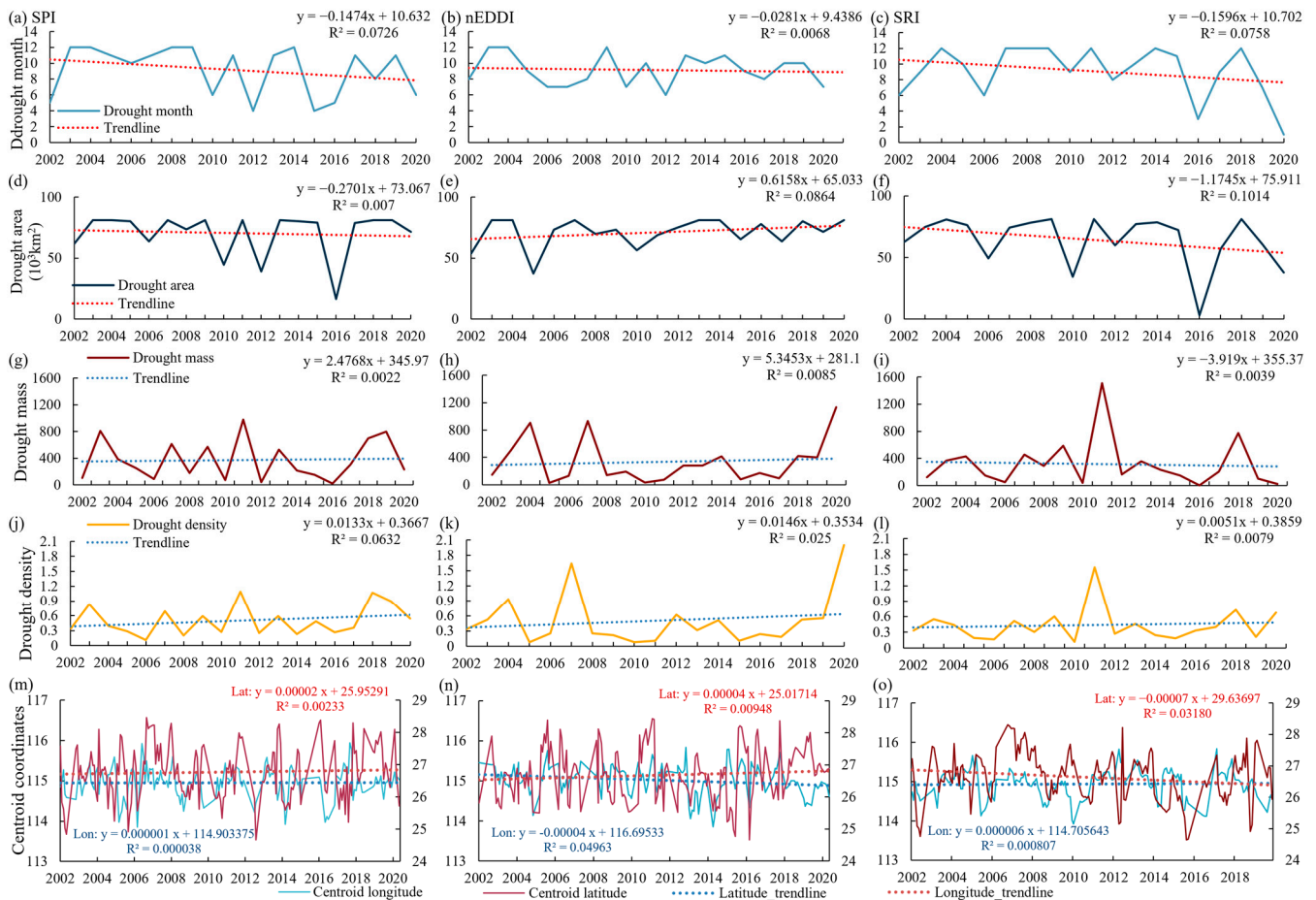


Figure 5. Temporal changes and trends of drought characteristics extracted from meteorological and hydrological drought events in the GRB from 2002 to 2020. The first (a,d,g,j,m), second (b,e,h,k,n) and third (c,f,i,l,o) columns are the drought characteristics of drought events extracted by SPI3, nEDDI3 and SRI3, respectively.

3.4. Response Characteristics of Meteorological Drought, Hydrological Drought and Vegetation

3.4.1. Response Time of Hydrological Drought to Meteorological Drought

Figure 7 presents the monthly correlations of SRI-SPI/nEDDI and NDVI-SPI/nEDDI/SRI at different scales from 2002 to 2020. In Figure 7a,b, the correlation results of SRI-SPI and SRI-nEDDI indicate the highest correlation coefficients of 0.96 and 0.57, respectively. The high correlation group of SRI-SPI generally exhibits significantly higher correlation coefficients compared to the high correlation group of SRI-nEDDI. This finding highlights that the correlation between hydrological drought and meteorological drought caused by insufficient precipitation in the GRB is substantially stronger than the correlation resulting from high temperature.

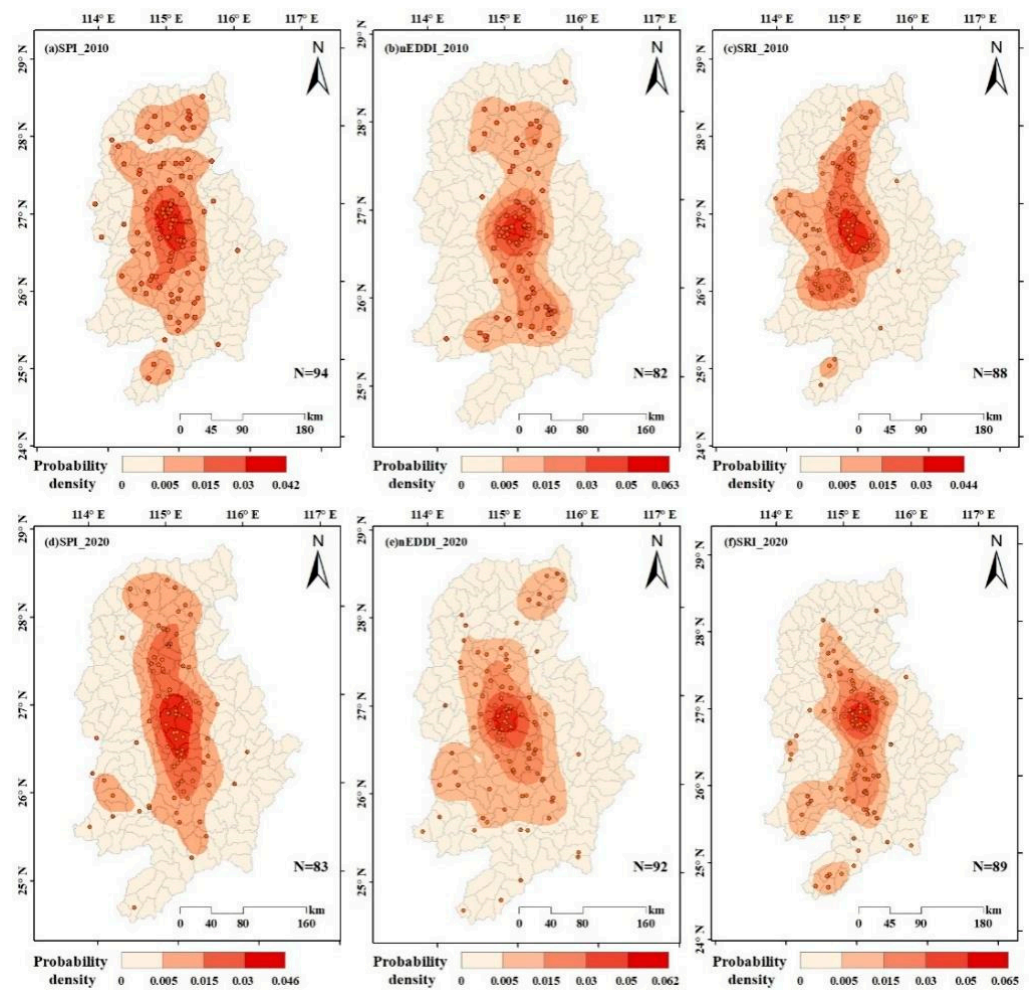


Figure 6. The distribution of weighted kernel density of drought centroids (the area of drought patch as weight) in meteorological and hydrological drought events in Ganjiang River Basin. (a–c) drought centroids in drought events identified by SPI, nEDDI and SRI from 2002 to 2010, (d–f) drought centroids in drought events identified by SPI, nEDDI and SRI from 2011 to 2020. The dots represent the centroid position of the drought patch.

Furthermore, it is evident that the response time of hydrological drought and meteorological drought varies across different seasons. In Figure 7a, the proportion of SRI-SPI correlation surpassing the 90% significance level test exceeded 48.9%, indicating a strong correlation between meteorological drought and hydrological drought caused by precipitation in the GRB. In spring (March–May), the response time of SRI to SPI was 1 month at the short-term scale and 12 months at the medium and long-term scale. The monthly response time is reduced from 12 months to 1 month. This reduction is attributed to the long-term winter rainfall scarcity in the GRB, resulting in insufficient surface water availability during early spring. As the rainy season commences in mid-March, precipitation intensity progressively increases, facilitating soil water and groundwater recharge and the formation of runoff. Considering that the MCC of SRI-SPI indicates the value at the 1-month scale in spring, the response time of spring is 1 month. In Figure 7b, the gradual increase in surface evapotranspiration associated with rising spring temperature initiates the vegetation growth period and contributes to an increase in vegetation evapotranspiration. This leads to a gradual increase in the correlation of SRI-nEDDI, which becomes significant in May. The response time for this period is 1 month. In summer (June–August), the response time of SRI to SPI is 6 months on the short-term scale, 12 months on the long-term scale. The response time of summer is 6 months. This longer response time is attributed to the peak vegetation growth and increased water consumption during this

period. The influence of subtropical high-pressure weather in July and August, characterized by high temperatures and limited rainfall, reduces soil moisture and groundwater, resulting in an extended response time from meteorological drought caused by insufficient precipitation to hydrological drought. The annual peak evapotranspiration in the basin, driven by subtropical high-pressure weather, accelerates surface and soil moisture loss due to vigorous vegetation transpiration. Thus, there is a significant relationship between hydrological drought and meteorological drought attributed to evapotranspiration during summer, with a response time of 6 months. In autumn and winter, the decreased precipitation extends the propagation time from meteorological drought to hydrological drought, increasing from 6 months in autumn to 12 months in winter. The continuous limited rainfall in autumn not only fails to replenish surface and soil moisture depleted by summer's high temperatures and evapotranspiration but also coincides with increased sunshine duration and evaporation capacity. Under the combined effect, there was a significant correlation observed between SRI and nEDDI in autumn, with a higher proportion of correlations exceeding the 95% significance level compared to summer. The monthly response time was extended from 3 months to 12 months, with a response time of 3 months for autumn. Although rainfall remains limited in winter, the sharp decrease in temperature leads to reduced evapotranspiration. However, the lack of surface and soil moisture replenishment in summer and autumn keeps the riverbed of the lower reaches of the GRB often barren in winter. As a result, the correlation between SRI and nEDDI in winter continues to decrease, and the response time of winter extends to 12 months.

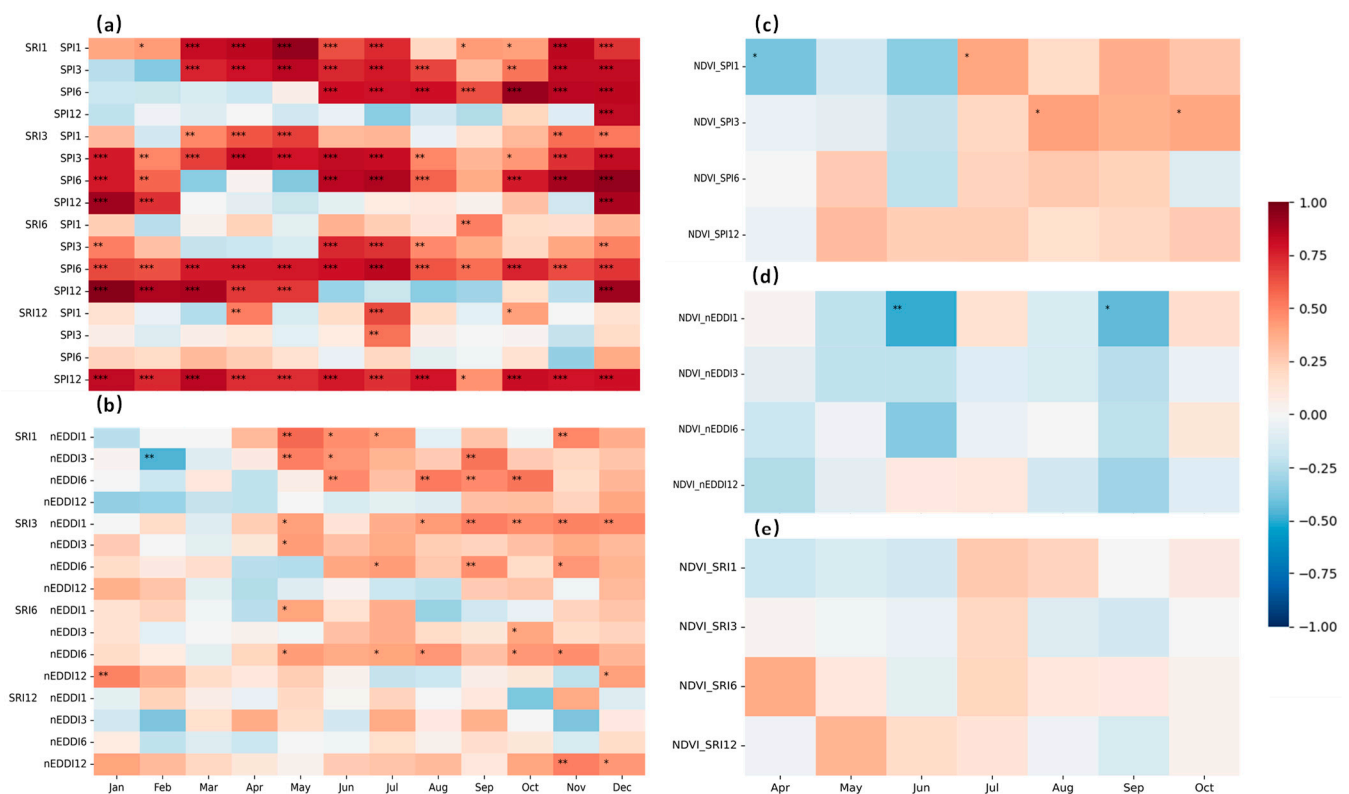


Figure 7. The correlation coefficients of SRI- n and SPI- n /nEDDI- n , monthly NDVI and SPI- n /nEDDI- n /SRI- n ($n = 1, 3, 6, 12$) from 2002 to 2020 in the GRB. *, **, *** represent that the correlation passes the significance level test of 90%, 95% and 99%, respectively. (a–e) represents the correlation coefficients of SRI-SPI, SRI-nEDDI, NDVI-SPI, NDVI-nEDDI and NDVI-SRI, respectively.

The propagation time from SPI-based and nEDDI-based meteorological drought to hydrological drought, as indicated by SRI, ranges from 1 to 6 months, taking into account the different seasons in the GRB. The correlation coefficients and the proportion of correlations reaching the 90% significance level of SRI-SPI are significantly higher than those

of SRI-nEDDI. This suggests that hydrological drought in the GRB is more responsive to meteorological drought driven by precipitation compared to drought caused by evapotranspiration. The seasonal response time of hydrological drought and meteorological drought shows consistency in spring, summer, and winter.

3.4.2. Response Time of Vegetation Drought to Meteorological and Hydrological Drought

Figure 7c–e illustrates the correlation coefficient of NDVI-SPI/nEDDI/SRI at different scales (1, 3, 6, and 12 months) for each month of the vegetation growing season. In Figure 7c, with the onset of the rainy season in March, precipitation continues and intensity increases, reaching its peak in May. This abundant rainfall compensates for the soil moisture deficit caused by water scarcity in winter and saturates the soil moisture content, meeting the water requirements for accelerated vegetation growth as the vegetation growth period begins. As a result, the correlation coefficient between NDVI and SPI changed from negative to positive in May. From July to August, influenced by subtropical high pressure, vegetation evaporation demand for soil moisture reaches its peak, but the lack of precipitation leads to the loss of surface and soil moisture, resulting in inadequate water supply for vegetation growth. Consequently, the growth rate of vegetation slows down, and the correlation coefficient between NDVI and SPI exhibits a gradual increment from July to August, showing a significant correlation during this period. The response time for the vegetation growing season is 3 months.

In Figure 7d, NDVI and nEDDI exhibit a negative correlation throughout the entire vegetation growth period, with significant negative correlations in June and September. In June, as the temperature rapidly rises, vegetation evapotranspiration increases. However, since June is also the peak of annual precipitation, the soil is adequately moist, allowing it to compensate for vegetation evapotranspiration and meet the water requirements for vegetation growth. In September, the evapotranspiration is lower compared to August, resulting in slightly weakened vegetation transpiration. However, the soil moisture deficit caused by the influence of subtropical high-pressure weather remains unaddressed, leading to water scarcity for vegetation. These observations suggest that vegetation growth is highly responsive to precipitation rather than evapotranspiration.

In Figure 7e, the correlation coefficients between NDVI and SRI during the vegetation growing season did not pass the significance test. The MCC of NDVI-SRI appeared in April, significantly decreased in June, and continues to decline after a slight rebound in July and August. The response time is 6 months. These findings can be attributed to April being in the rainy season and the early stage of vegetation growth. Precipitation is intercepted by vegetation to satisfy the water requirements for vegetation growth and evapotranspiration, and then infiltrates into the soil to compensate for the long-term deficit of soil water caused by inadequate rainfall in winter. In June, the precipitation intensity reaches its peak, leading to near-saturation of surface water, while the growth rate of vegetation coverage experiences a slowdown. As a result, there is a reduction in the fraction of vegetation changes affecting hydrological processes. In July and August, there is a significant decrease in precipitation. However, the gradual expansion of plant coverage leads to an increase in evapotranspiration and precipitation interception, resulting in a decrease in runoff. Consequently, the correlation between NDVI and SRI increases in July and August. The notable decrease of NDVI from September to October leads to a decrease in the proportion of vegetation changes affecting hydrological processes.

3.4.3. Spatial Distribution Characteristics of Hydrological Response to Meteorological Drought

By calculating the correlation of SRI-SPI/nEDDI at multiple time scales, the MCC of each sub-basin is illustrated in Figure 8a,b. The corresponding seasons for the MCC are counted as shown in Figure 8c,d. The MCC between SPI and SRI ranges from 0.84 to 0.98 and passes the significance test at a 95% confidence level. In Figure 8b, the area with MCC in spring, summer, autumn, and winter account for 20%, 22%, 19%, and 39% of the total basin area, respectively. The results demonstrate that the meteorological drought resulting

from insufficient precipitation has the strongest impact on runoff in winter, and the impact area is mainly concentrated in the mountainous and hilly regions in the middle and upper basin sections.

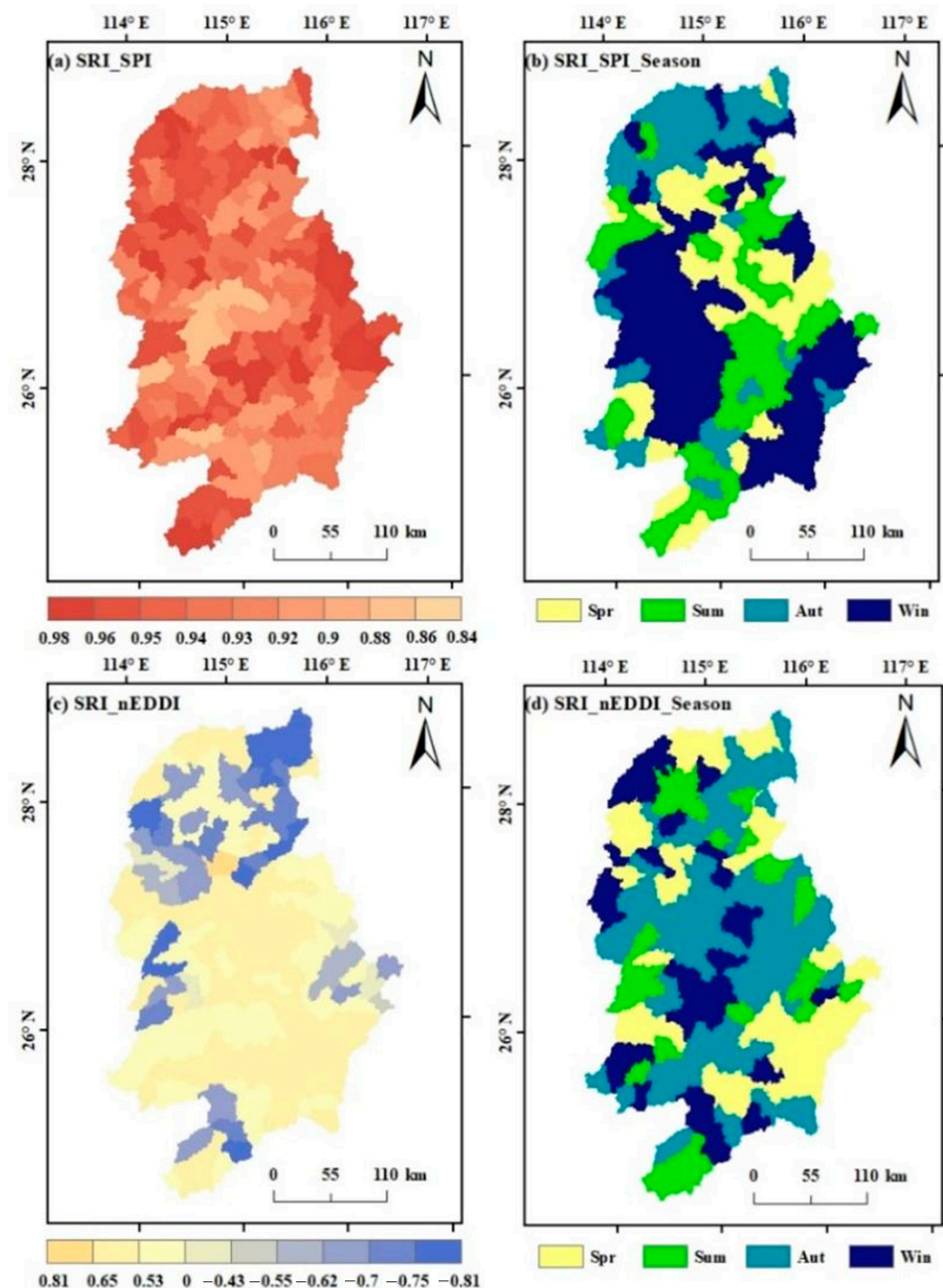


Figure 8. The maximum correlation coefficient distribution of multiscale SRI-SPI and SRI-nEDDI and the seasonal distribution of the maximum correlation coefficient in the GRB.

The MCC between nEDDI and SRI exhibits a range of -0.82 to 0.81 . The downstream region displays a notable concentration of negative MCC values, likely attributed to its smaller basin area and lower water levels. Conversely, positive MCC values are observed in the middle and upper reaches. Figure 8d depicts the distribution of MCC in different seasons, highlighting that the autumn MCC area encompasses 41% of the total basin area, followed by 25% in spring, 20% in winter, and 14% in summer. Notably, autumn contributes the most significantly among the seasons, with the region exhibiting the highest MCCs

closely aligning with this area. These results indicate that meteorological drought induced by autumn evapotranspiration poses the greatest threat to runoff in the GRB.

3.4.4. Spatial Distribution Characteristics of Vegetation Response to Meteorological and Hydrological Drought

Figure 9a–f illustrate the spatial distribution of the MCCs of NDVI-SPI/nEDDI/SRI and the monthly distribution of MCC. The MCCs of NDVI-SPI/nEDDI/SRI in the GRB are between -0.65 and 0.68 , -0.8 and 0.67 , and -0.72 and 0.69 , respectively.

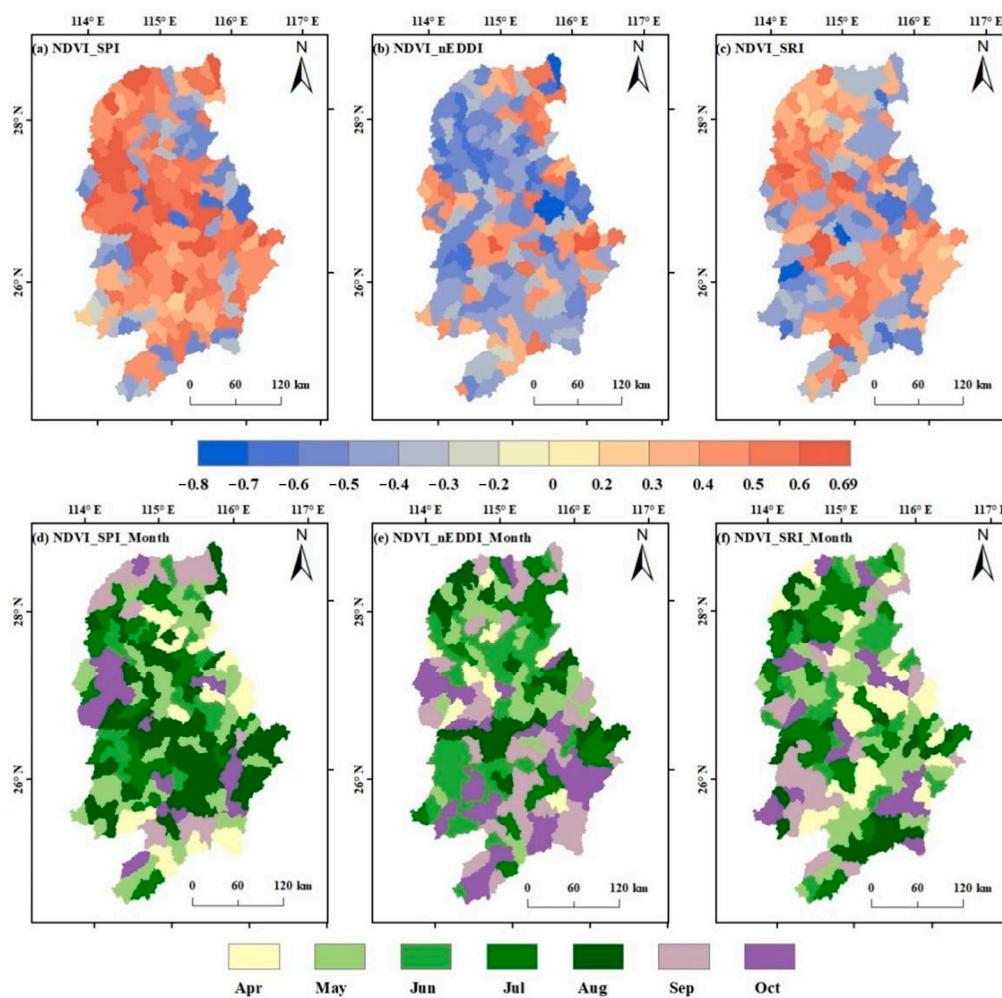


Figure 9. The maximum correlation coefficient distribution of monthly NDVI with SPI, nEDDI and SRI at different scales and the monthly distribution of the maximum correlation coefficient during the growing season of vegetation in the GRB.

The MCC between NDVI and SPI predominantly occurred in August, covering approximately 27% of the total basin area, followed by May, accounting for 20%. The August MCC area is mainly situated in the midstream and downstream regions, aligning with the region exhibiting the maximum MCC. In contrast, the May MCC area is scattered throughout the basin. The results suggest that the vegetation in the middle and lower sections of the basin, influenced by the subtropical high-pressure weather in August, is most susceptible to meteorological drought. Additionally, vegetation growth in the basin in May is significantly affected by precipitation.

The negative MCC between NDVI and nEDDI encompasses 69% of the total basin area. The positive MCC is distributed in the middle reaches and the western side of the downstream, consistent with the area where the MCC appeared in July. It is apparent that

the vegetation in the plain area of the lower reaches of the basin is highly sensitive to the summer subtropical high-pressure weather.

The positive MCC between NDVI and SRI is primarily distributed in the midwest of the upstream and the mid-east of the downstream, with scattered occurrences in the middle reaches. The area with the MCC in May and July both account for 19% of the total basin area. This distribution pattern aligns closely with the distribution of the positive MCC, indicating that the hydrological drought in May and July will exert a greater impact on vegetation.

3.5. Dynamic Relationship among Meteorology, Hydrology and Vegetation Drought

As the revealed correlation results between SRI, SPI, nEDDI and NDVI in Figure 7, the index pairs with the MCC were selected for XWT and WTC analysis to determine the propagation relationship between different droughts in time-frequency space.

3.5.1. Cross-Wavelet Transform and Wavelet Coherence between the SRI and the SPI/EDDI

In Figure 10, the XWT and WTC results between SRI and SPI/nEDDI, with the highest correlation in the GRB from 2002 to 2020, are presented. From the XWT results of SRI and SPI in Figure 10a–d, it is observed that from April 2008 to January 2015, SRI1 and SPI1 exhibited resonance with a period of 20–50 months. The duration of the resonance prolongs as the SRI time scale increases. Moreover, intermittent short-term resonances between SRI and SPI occur within the 0–10 month period. At each time scale, SRI and SPI display a significant in-phase relationship across various periodic scales, with SRI generally lagging behind SPI by 3 to 118 days. Figure 10e–h display the WTC results for SRI and SPI. Compared to the XWT analysis, SRI and SPI demonstrate a pronounced in-phase relationship in most regions, particularly at the 12-month scale. The resonance period spans from 0 to 72 months. These findings indicate that the strong correlation between SRI and SPI can also be detected in the low-frequency domain. This further emphasizes the significant and consistent correlation between meteorological drought and hydrological drought caused by water shortage in the GRB.

Figure 10i–l presents the XWT results of SRI and nEDDI. The analysis indicates a significant correlation between SRI and nEDDI, primarily manifested in the resonance of SRI1 and nEDDI1 over a period of 20–31 months from January 2007 to June 2011. The duration of this resonance also increases with the scaling up of SRI. In addition, there are intermittent quasi-periodic resonances in the period of 0–5 months. At each periodic scale, SRI exhibits a significant in-phase relationship with nEDDI, with a lag time between 2–224 days. In Figure 10m–p, which displays the WTC results for SRI and nEDDI, intermittent resonance dominates with a period ranging from 0 to 16 months, revealing a significant in-phase relationship. These findings indicate that a high coherence can also be detected between SRI and nEDDI in the low-frequency domain. However, it is important to note that the relationship between these two indices is not stable. Based on the XWT and WTC results of SRI and nEDDI, it is evident that the meteorological drought caused by evapotranspiration acts as the driving factor of hydrological drought in the GRB, but the relationship between these two types of drought is comparatively more unstable than the relationship between meteorological drought caused by insufficient precipitation.

3.5.2. Cross-Wavelet Transform and Wavelet Coherence between the NDVI and the SPI/EDDI/SRI

Figure 11a–f show the cross-wavelet spectrum and wavelet coherence of monthly NDVI with SPI/nEDDI/SRI in the GRB from 2002 to 2020. In Figure 11a–c, a significant correlation exists between changes in vegetation cover and meteorological/hydrological drought in the GRB. This observation is supported by the presence of a resonance region with a significance level of 95%, which spans 7 to 15 months for NDVI and its correlations with SPI3, nEDDI1, and SRI6. The time periods showcasing the resonance region for NDVI and SPI3 at this periodic scale range from May 2005 to January 2007, March 2011

to February 2013, and June 2016 to September 2019. At this periodic scale, the resonance between NDVI and nEDDI1 is more concentrated, spanning from August 2003 to March 2015. The resonance periods for NDVI and SRI6 at this periodic scale last from January 2003 to May 2010 and from January 2011 to May 2019, respectively. An intermittent short-term resonance between NDVI and the three indices occurs within the 0–6 month period. NDVI exhibited time lags of 1–208 days, 12–163 days, and 1–172 days with respect to SPI3, nEDDI1, and SRI6. Figure 11d–f reveal intermittent resonances, with a significance level of 95% between NDVI and SPI3/nEDDI1/SRI6 in the 0–14 month period. These findings support the presence of a significant correlation between changes in vegetation cover and meteorological/hydrological drought in the low-frequency domain, but this correlation may be affected by seasonal and other factors, introducing potential instability.

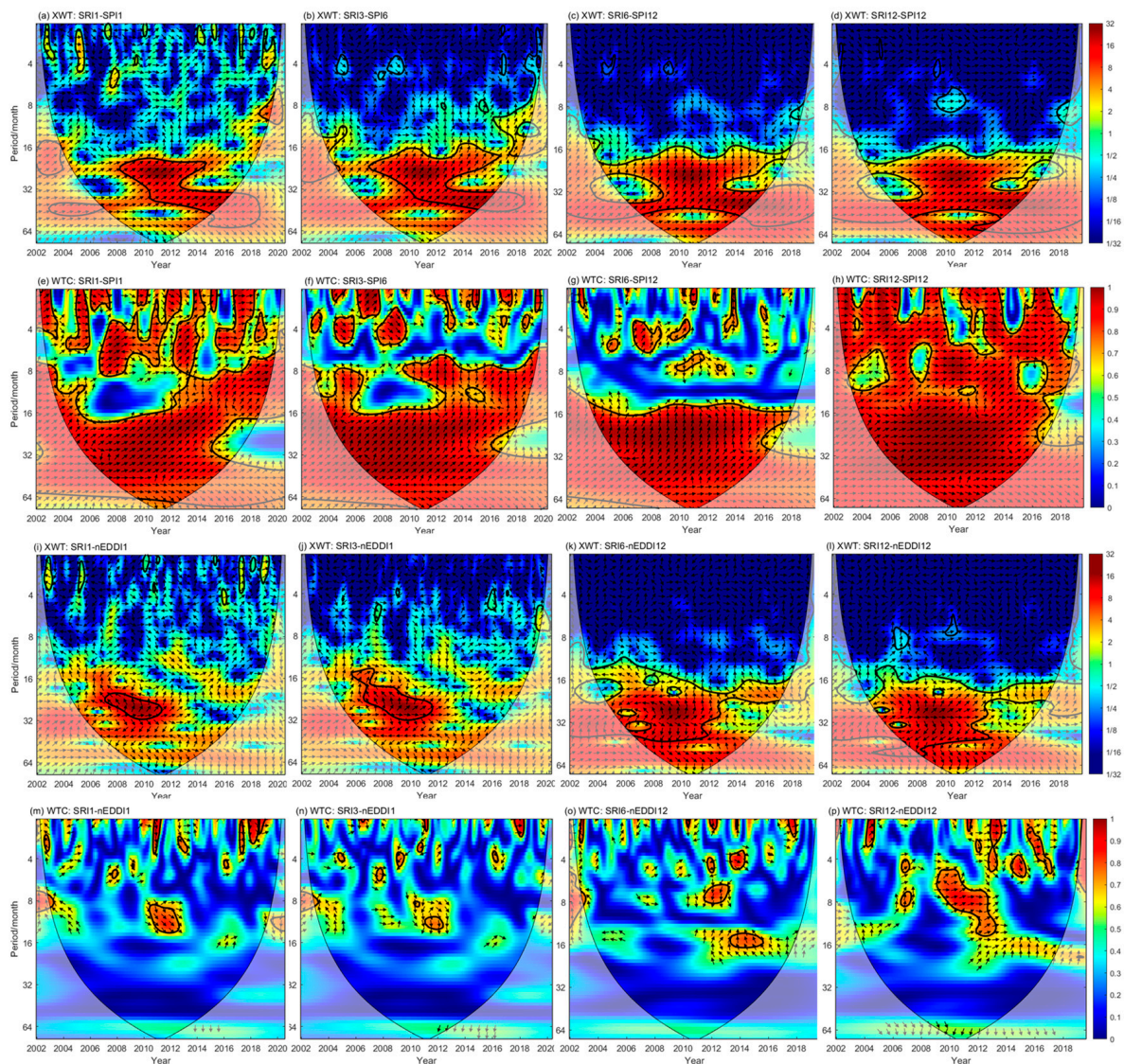


Figure 10. Cross-wavelet power spectrum and wavelet coherence of SRIn ($n = 1, 3, 6, 12$) with SPI and nEDDI in the GRB from 2002 to 2020. (a–d) XWT of SRI with SPI, (e–h) WTC of SRI with SPI, (i–l) XWT of SRI with nEDDI, (m–p) WTC of SRI with nEDDI. The black contour represents the significant power region for the red noise at the 95% confidence level. The influence cone COI (black curve) represents the region without edge effect. The power value from dark blue to deep red indicates low power to high power. The arrow indicates the phase information in the time–frequency domain, and the direction of the arrow indicates the phase difference.

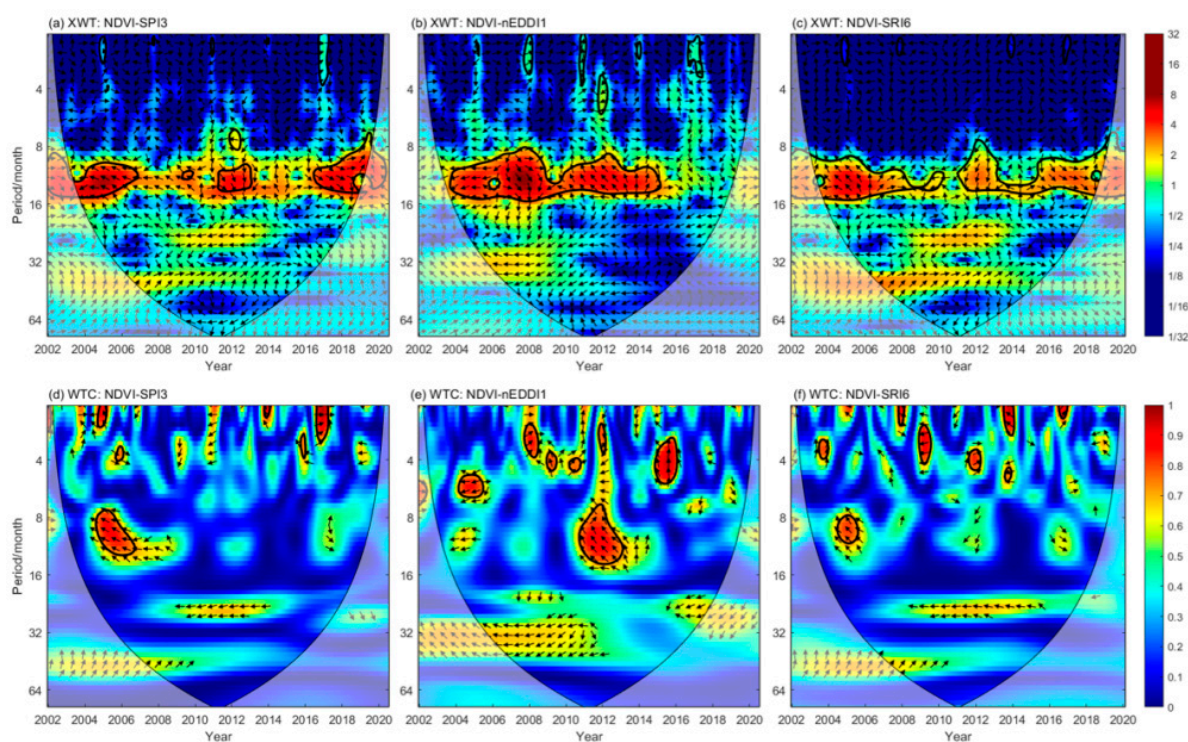


Figure 11. Cross-wavelet power spectrum and wavelet coherence between NDVI and SPI3, nEDDI1, and SRI6 in the GRB from 2002 to 2020. (a–c) XWT of NDVI with SPI3, nEDDI1, and SRI6, (d–f) WTC of NDVI with SPI3, nEDDI1, and SRI6.

4. Discussion

Thorough and meticulous research in drought monitoring plays a crucial role in acquiring accurate and comprehensive information necessary for effective drought response and reliable data support. It also aids in assessing drought mechanisms and understanding ecological environments. While statistical probability-based indices are widely used in drought monitoring, they primarily rely on site-specific data and may overlook the impact of regional factors and complex interactions among various physical components [90,91]. To address this limitation, integrating drought indices with distributed hydrological models has emerged as a more robust methodology for comprehensive understanding and effective monitoring of drought [92,93]. In this study, the GRB was divided into 172 sub-watersheds using a slope runoff simulation algorithm. Hydrometeorology and multi-source data were utilized to simulate the ET and runoff of each sub-watershed employing PML _ V2 and SWAT model. To validate the reliability of the model simulation, the simulated ET and runoff were compared with the field data, confirming their accuracy. Subsequently, drought indices, including SPI, EDDI, SRI, and NDVI, were calculated for each sub-basin. This approach stands as a valuable reference for obtaining drought indices that closely align with actual conditions in non-stationary areas or when additional physical factors need to be considered.

With increasing accessibility to data, there has been a growing emphasis on studying the entire chain of drought propagation. The scope of drought propagation research has expanded beyond meteorological to hydrological (or agricultural) drought. Notably, scholars have investigated the propagation patterns and features of meteorological, hydrological, and agricultural droughts in various climatic regions and major river basins in China [48,50]. Some studies have even utilized Gravity Recovery and Climate Experiment (GRACE) data to further explore hydrological droughts by categorizing them into surface runoff droughts and groundwater droughts [49,94]. In consideration of the trend of climate warming, this study investigated the response time and propagation relationships between meteorological drought caused by various factors to hydrological/vegetation droughts,

as well as the propagation of hydrological drought to vegetation drought. The findings significantly contribute to the early identification of drought propagation occurrences. The variability in drought response time, influenced by seasonal factors, enables a quantitative assessment of risks and vulnerabilities associated with drought propagation across different regions and seasons. This analysis also provides critical information for predicting and evaluating the impact of drought, especially on crop yield, the ecological vitality of forests and wetlands, and overall biodiversity resilience. As a result of data limitations, this paper does not conduct in-depth research on the spread of groundwater drought. Nevertheless, it is noteworthy to acknowledge that groundwater plays a crucial role in recharging surface water during the dry season in the GRB. The availability of groundwater significantly impacts vegetation and soil moisture in the basin. Hence, future research endeavors will encompass the collection of GRACE data and in-situ groundwater data to investigate the relationship between groundwater drought and other types of drought.

Furthermore, we address the spatial–temporal coupling of drought by implementing a robust three-dimensional clustering method. This approach allows us to extract 3D drought events and their drought characteristics (duration, area, severity, centroid, etc.) [95]. Utilizing this method offers advantages in describing and quantifying the development and evolution characteristics of drought events, eliminating the dependence on subjective regional thresholds that previous studies relied on [76]. Given the constraints of this article, we have not explicitly examined the relationship between the drought characteristics of different drought types. In future research, we propose utilizing a response function model such as the copula model to investigate the propagation relationship between drought characteristics, facilitating the exploration of the propagation mechanism from the standpoint of drought propagation probabilities.

Drought spreads through the interrelated land-atmosphere system and hydrological cycle process and evolves into different types of drought in different geographical locations and time periods. This progression often initiates with meteorological drought, which is virtually impossible to prevent. However, through a systematic understanding of drought response mechanisms, proactive measures can be implemented to prevent or mitigate the spread of meteorological drought to agricultural, hydrological, and socio-economic drought, thereby reducing its detrimental impact and preventing further expansion of the spread process. In the case of the GRB, a notable correlation is observed between the nEDDI and SRI in the central region during autumn. During episodes of persistent high evaporation in autumn, it is crucial for the aforementioned areas to focus on timely water storage within the basin.

5. Conclusions

This study introduces the use of SPI, EDDI, SRI, and NDVI to analyze and evaluate the spatial–temporal evolution characteristics of meteorological, hydrological and vegetation drought in the GRB from 2002 to 2020, as well as their variations across different seasons. The investigation focuses on examining the spatial–temporal response of hydrological drought to meteorological drought and vegetation drought to meteorological/hydrological drought at various time scales using methods such as MCC and Cross-Wavelet transform. The main conclusions of this study are as follows:

(1) From 2002 to 2020, the SPI-based meteorological drought and hydrological drought in the GRB exhibited a decelerating tendency, particularly in terms of drought frequency and extent, while the overall development trend of EDDI-based meteorological drought was severe. SPI drought generally gathers in the central region, and SRI drought tends to migrate towards the south. EDDI drought has a tendency to migrate northwestward.

(2) Meteorological and hydrological drought in the GRB are closely related, especially the meteorological drought caused by precipitation. The propagation time exhibits obvious seasonal differences. The propagation time of SPI-SRI was the shortest in spring, extended in summer and autumn, and the longest in winter. The SPI drought in winter had the strongest impact on hydrological drought, and the affected areas were predominantly

located in the mountainous and hilly areas in the middle and upper reaches of the basin. The propagation time of EDDI-SRI was consistent with SPI-SRI in spring, summer and winter, while the propagation time in autumn was slightly less than that in summer. The EDDI drought in autumn had the strongest impact on hydrological drought, and the affected areas were widely distributed in the basin.

(3) The correlation between vegetation drought and meteorological drought caused by precipitation in the GRB is the highest. During the growing season, NDVI and SPI had the highest correlation in August, and the affected areas were widely distributed in the middle and upper reaches of the basin. The areas with high correlation between NDVI and SRI are distributed in the northwest and southeast of the basin. The correlation between NDVI and EDDI is typically weak within the basin, indicating that meteorological drought caused by high evapotranspiration is not the main factor affecting vegetation growth.

(4) There are similar periodic variation patterns among meteorological, hydrological, and vegetation drought in the GRB. The SPI and SRI have significant resonance periods in 0–10 months and 20–50 months, and the lag time is between 3–118 days. The EDDI and SRI have significant resonance periods in 0–5 months and 20–31 months, and the lag time is between 2–224 days. The short-term resonance period is intermittent, while the long-term is stable. Similarly, vegetation drought and meteorological/hydrological drought have significant intermittent resonance periods in 0~6 months and significant stable resonance periods in 7~15 months. NDVI lagged behind SPI, EDDI and SRI by 1–208 days, 12–163 days and 1–172 days, respectively.

Author Contributions: Conceptualization, S.Z.; methodology, W.H.; validation, X.L. and J.G.; resources, Z.Y.; writing—original draft preparation, S.Z. and W.H.; writing—review and editing, X.L. and J.G.; funding acquisition, Z.Y. All authors have read and agreed to the published version of the manuscript.

Funding: This study is supported by the National Natural Science Foundation of China, No. 52109004 and 52079008.

Data Availability Statement: The datasets used or analyzed during the current study are available from the corresponding author on reasonable request.

Conflicts of Interest: The authors declare no conflict of interest.

References

- Zhang, X.; Hao, Z.; Singh, V.P.; Zhang, Y.; Feng, S.; Xu, Y.; Hao, F. Drought propagation under global warming: Characteristics, approaches, processes, and controlling factors. *Sci. Total Environ.* **2022**, *838*, 156021. [\[CrossRef\]](#)
- Mishra, A.K.; Singh, V.P. A review of drought concepts. *J. Hydrol.* **2010**, *391*, 202–216. [\[CrossRef\]](#)
- Xu, Y.; Zhang, X.; Hao, Z.; Singh, V.P.; Hao, F. Characterization of agricultural drought propagation over China based on bivariate probabilistic quantification. *J. Hydrol.* **2021**, *598*, 126194. [\[CrossRef\]](#)
- Willhite, D.A. *Drought and Water Crises: Science, Technology, and Management Issues*; CRC Press: Boca Raton, FL, USA, 2005.
- Eltahir, E.A.B.; Yeh, P.J.F. On the asymmetric response of aquifer water level to floods and droughts in Illinois. *Water Resour. Res.* **1999**, *35*, 1199–1217. [\[CrossRef\]](#)
- Changnon, S.A. *Detecting Drought Conditions in Illinois*; Circular 169; Illinois State Water Survey: Champaign, IL, USA, 1987.
- Heudorfer, B.; Stahl, K. Comparison of different threshold level methods for drought propagation analysis in Germany. *Hydrol. Res.* **2016**, *48*, 1311–1326. [\[CrossRef\]](#)
- Wang, W.; Ertsen, M.W.; Svoboda, M.D.; Hafeez, M. Propagation of Drought: From Meteorological Drought to Agricultural and Hydrological Drought. *Adv. Meteorol.* **2016**, *2016*, 6547209. [\[CrossRef\]](#)
- Rajsekhar, D.; Singh, V.P.; Mishra, A.K. Multivariate drought index: An information theory based approach for integrated drought assessment. *J. Hydrol.* **2015**, *526*, 164–182. [\[CrossRef\]](#)
- McKee, T.B.; Doesken, N.J.; Kleist, J.R. The relationship of drought frequency and duration to time scales. In Proceedings of the 8th Conference on Applied Climatology, Anaheim, CA, USA, 17–22 January 1993.
- Vicente-Serrano, S.M.; Beguería, S.; López-Moreno, J.I. A Multiscalar Drought Index Sensitive to Global Warming: The Standardized Precipitation Evapotranspiration Index. *J. Clim.* **2010**, *23*, 1696–1718. [\[CrossRef\]](#)
- Hobbins, M.T.; Wood, A.; McEvoy, D.J.; Huntington, J.L.; Morton, C.; Anderson, M.; Hain, C. The Evaporative Demand Drought Index. Part I: Linking Drought Evolution to Variations in Evaporative Demand. *J. Hydrometeorol.* **2016**, *17*, 1745–1761. [\[CrossRef\]](#)
- Farahmand, A.; AghaKouchak, A. A generalized framework for deriving nonparametric standardized drought indicators. *Adv. Water Resour.* **2015**, *76*, 140–145. [\[CrossRef\]](#)

14. Li, L.; She, D.; Zheng, H.; Lin, P.; Yang, Z.-L. Elucidating Diverse Drought Characteristics from Two Meteorological Drought Indices (SPI and SPEI) in China. *J. Hydrometeorol.* **2020**, *21*, 1513–1530. [[CrossRef](#)]
15. Wang, Y.-R.; Hessen, D.O.; Samset, B.H.; Stordal, F. Evaluating global and regional land warming trends in the past decades with both MODIS and ERA5-Land land surface temperature data. *Remote Sens. Environ.* **2022**, *280*, 113181. [[CrossRef](#)]
16. Yin, S.-Y.; Wang, T.; Hua, W.; Miao, J.-P.; Gao, Y.-Q.; Fu, Y.-H.; Matei, D.; Tyrlis, E.; Chen, D. Mid-summer surface air temperature and its internal variability over China at 1.5 °C and 2 °C global warming. *Adv. Clim. Change Res.* **2020**, *11*, 185–197. [[CrossRef](#)]
17. Vicente-Serrano, S.M.; Van der Schrier, G.; Beguería, S.; Azorin-Molina, C.; Lopez-Moreno, J.-I. Contribution of precipitation and reference evapotranspiration to drought indices under different climates. *J. Hydrol.* **2015**, *526*, 42–54. [[CrossRef](#)]
18. Haile, G.G.; Tang, Q.H.; Hosseini-Moghari, S.M.; Liu, X.C.; Gebremicael, T.G.; Leng, G.Y.; Kebede, A.; Xu, X.M.; Yun, X.B. Projected Impacts of Climate Change on Drought Patterns Over East Africa. *Earths Future* **2020**, *8*, e2020EF001502. [[CrossRef](#)]
19. Zheng, Y.X.; Zhang, X.; Yu, J.S.; Xu, Y.; Wang, Q.Y.; Li, C.; Yao, X.L. Assessing the Joint Impact of Climatic Variables on Meteorological Drought Using Machine Learning. *Front. Earth Sci.* **2022**, *10*, 835142. [[CrossRef](#)]
20. McEvoy, D.J.; Huntington, J.L.; Hobbins, M.T.; Wood, A.; Morton, C.; Anderson, M.; Hain, C. The Evaporative Demand Drought Index. Part II: CONUS-Wide Assessment against Common Drought Indicators. *J. Hydrometeorol.* **2016**, *17*, 1763–1779. [[CrossRef](#)]
21. Yao, N.; Li, Y.; Lei, T.; Peng, L. Drought evolution, severity and trends in mainland China over 1961–2013. *Sci. Total Environ.* **2018**, *616–617*, 73–89. [[CrossRef](#)]
22. Chen, N.; Li, R.; Zhang, X.; Yang, C.; Wang, X.; Zeng, L.; Tang, S.; Wang, W.; Li, D.; Niyogi, D. Drought propagation in Northern China Plain: A comparative analysis of GLDAS and MERRA-2 datasets. *J. Hydrol.* **2020**, *588*, 125026. [[CrossRef](#)]
23. Van Loon, A.F. Hydrological drought explained. *Wiley Interdiscip. Rev.-Water* **2015**, *2*, 359–392. [[CrossRef](#)]
24. Guo, J.; Liu, Y.; Zou, Q.; Ye, L.; Zhu, S.; Zhang, H. Study on optimization and combination strategy of multiple daily runoff prediction models coupled with physical mechanism and LSTM. *J. Hydrol.* **2023**, *624*, 129969. [[CrossRef](#)]
25. Shukla, S.; Wood, A. Use of a standardized runoff index for characterizing hydrologic drought. *Geophys. Res. Lett.-Geophys. Res. Lett.* **2008**, *35*. [[CrossRef](#)]
26. Liu, X.; Zhu, X.; Pan, Y.; Li, S.; Liu, Y.; Ma, Y. Agricultural drought monitoring: Progress, challenges, and prospects. *J. Geogr. Sci.* **2016**, *26*, 750–767. [[CrossRef](#)]
27. Li, R.; Tsunekawa, A.; Tsubo, M. Assessment of agricultural drought in rainfed cereal production areas of northern China. *Theor. Appl. Climatol.* **2017**, *127*, 597–609. [[CrossRef](#)]
28. Palmer, W. *Meteorological Drought*; Research Paper No. 45; U.S. Department of Commerce: Washington, DC, USA, 1965.
29. Paulo, A.A.; Pereira, L.S. Drought concepts and characterization: Comparing drought indices applied at local and regional scales. *Water Int.* **2006**, *31*, 37–49. [[CrossRef](#)]
30. Shen, Z.; Zhang, Q.; Singh, V.P.; Sun, P.; Song, C.; Yu, H. Agricultural drought monitoring across Inner Mongolia, China: Model development, spatiotemporal patterns and impacts. *J. Hydrol.* **2019**, *571*, 793–804. [[CrossRef](#)]
31. Rouse, J.W.; Haas, R.H.; Schell, J.A.; Deering, D.W. Monitoring vegetation systems in the great plains with ERTS. *NASA Spec. Publ.* **1973**, *351*, 309.
32. Fang, W.; Huang, S.Z.; Huang, Q.; Huang, G.H.; Wang, H.; Leng, G.Y.; Wang, L.; Guo, Y. Probabilistic assessment of remote sensing-based terrestrial vegetation vulnerability to drought stress of the Loess Plateau in China. *Remote Sens. Environ.* **2019**, *232*, 111290. [[CrossRef](#)]
33. Hu, X.B.; Ren, H.Z.; Tansey, K.; Zheng, Y.T.; Ghent, D.; Liu, X.F.; Yan, L. Agricultural drought monitoring using European Space Agency Sentinel 3A land surface temperature and normalized difference vegetation index imageries. *Agric. For. Meteorol.* **2019**, *279*, 107707. [[CrossRef](#)]
34. Ji, L.; Peters, A.J. Assessing vegetation response to drought in the northern Great Plains using vegetation and drought indices. *Remote Sens. Environ.* **2003**, *87*, 85–98. [[CrossRef](#)]
35. Zhou, Z.Q.; Shi, H.Y.; Fu, Q.; Ding, Y.B.; Li, T.X.; Liu, S.N. Investigating the Propagation From Meteorological to Hydrological Drought by Introducing the Nonlinear Dependence With Directed Information Transfer Index. *Water Resour. Res.* **2021**, *57*, e2021WR030028. [[CrossRef](#)]
36. Li, Q.F.; He, P.F.; He, Y.C.; Han, X.Y.; Zeng, T.S.; Lu, G.B.; Wang, H.J. Investigation to the relation between meteorological drought and hydrological drought in the upper Shaying River Basin using wavelet analysis. *Atmos. Res.* **2020**, *234*, 104743. [[CrossRef](#)]
37. Guo, Y.; Huang, S.Z.; Huang, Q.; Leng, G.Y.; Fang, W.; Wang, L.; Wang, H. Propagation thresholds of meteorological drought for triggering hydrological drought at various levels. *Sci. Total Environ.* **2020**, *712*, 136502. [[CrossRef](#)]
38. Dai, M.; Huang, S.Z.; Huang, Q.; Zheng, X.D.; Su, X.L.; Leng, G.Y.; Li, Z.Y.; Guo, Y.; Fang, W.; Liu, Y.J. Propagation characteristics and mechanism from meteorological to agricultural drought in various seasons. *J. Hydrol.* **2022**, *610*, 127897. [[CrossRef](#)]
39. Wang, F.; Lai, H.X.; Li, Y.B.; Feng, K.; Zhang, Z.Z.; Tian, Q.Q.; Zhu, X.M.; Yang, H.B. Dynamic variation of meteorological drought and its relationships with agricultural drought across China. *Agric. Water Manag.* **2022**, *261*, 107301. [[CrossRef](#)]
40. Zampieri, M.; D Andrea, F.; Vautard, R.; Ciais, P.; de Noblet-Ducoudré, N.; Yiou, P. Hot European Summers and the Role of Soil Moisture in the Propagation of Mediterranean Drought. *J. Clim.* **2009**, *22*, 4747–4758. [[CrossRef](#)]
41. Van Lanen, H.A.J.; Wanders, N.; Tallaksen, L.M.; Van Loon, A.F. Hydrological drought across the world: Impact of climate and physical catchment structure. *Hydrol. Earth Syst. Sci.* **2013**, *17*, 1715–1732. [[CrossRef](#)]
42. Van Loon, A.F.; Laaha, G. Hydrological drought severity explained by climate and catchment characteristics. *J. Hydrol.* **2015**, *526*, 3–14. [[CrossRef](#)]

43. Van Loon, A.F.; Van Lanen, H.A.J. A process-based typology of hydrological drought. *Hydrol. Earth Syst. Sci.* **2012**, *16*, 1915–1946. [[CrossRef](#)]
44. Van Loon, A.F.; Tijdeman, E.; Wanders, N.; Van Lanen, H.A.J.; Teuling, A.J.; Uijlenhoet, R. How climate seasonality modifies drought duration and deficit. *J. Geophys. Res.-Atmos.* **2014**, *119*, 4640–4656. [[CrossRef](#)]
45. Geyaert, A.I.; Veldkamp, T.I.E.; Ward, P.J. The effect of climate type on timescales of drought propagation in an ensemble of global hydrological models. *Hydrol. Earth Syst. Sci.* **2018**, *22*, 4649–4665.
46. Apurv, T.; Sivapalan, M.; Cai, X.M. Understanding the Role of Climate Characteristics in Drought Propagation. *Water Resour. Res.* **2017**, *53*, 9304–9329. [[CrossRef](#)]
47. Pan, Z.K.; Liu, P.; Xu, C.Y.; Cheng, L.; Tian, J.; Cheng, S.J.; Xie, K. The influence of a prolonged meteorological drought on catchment water storage capacity: A hydrological-model perspective. *Hydrol. Earth Syst. Sci.* **2020**, *24*, 4369–4387. [[CrossRef](#)]
48. Ding, Y.B.; Gong, X.L.; Xing, Z.X.; Cai, H.J.; Zhou, Z.Q.; Zhang, D.D.; Sun, P.; Shi, H.Y. Attribution of meteorological, hydrological and agricultural drought propagation in different climatic regions of China. *Agric. Water Manag.* **2021**, *255*, 106996. [[CrossRef](#)]
49. Zhang, H.; Ding, J.; Wang, Y.; Zhou, D.; Zhu, Q. Investigation about the correlation and propagation among meteorological, agricultural and groundwater droughts over humid and arid/semi-arid basins in China. *J. Hydrol.* **2021**, *603*, 127007. [[CrossRef](#)]
50. Um, M.-J.; Kim, Y.; Jung, K.; Lee, M.; An, H.; Min, I.; Kwak, J.; Park, D. Evaluation of drought propagations with multiple indices in the Yangtze River basin. *J. Environ. Manag.* **2022**, *317*, 115494. [[CrossRef](#)]
51. Huang, S.; Li, P.; Huang, Q.; Leng, G.; Hou, B.; Ma, L. The propagation from meteorological to hydrological drought and its potential influence factors. *J. Hydrol.* **2017**, *547*, 184–195. [[CrossRef](#)]
52. Li, R.H.; Chen, N.C.; Zhang, X.; Zeng, L.L.; Wang, X.P.; Tang, S.J.; Li, D.R.; Niyogi, D. Quantitative analysis of agricultural drought propagation process in the Yangtze River Basin by using cross wavelet analysis and spatial autocorrelation. *Agric. For. Meteorol.* **2020**, *280*, 107809. [[CrossRef](#)]
53. Edossa, D.C.; Babel, M.S.; Das Gupta, A. Drought Analysis in the Awash River Basin, Ethiopia. *Water Resour. Manag.* **2010**, *24*, 1441–1460. [[CrossRef](#)]
54. Wu, J.F.; Chen, X.W.; Yao, H.X.; Gao, L.; Chen, Y.; Liu, M.B. Non-linear relationship of hydrological drought responding to meteorological drought and impact of a large reservoir. *J. Hydrol.* **2017**, *551*, 495–507. [[CrossRef](#)]
55. Wong, G.; van Lanen, H.A.J.; Torfs, P. Probabilistic analysis of hydrological drought characteristics using meteorological drought. *Hydrol. Sci. J.-J. Des Sci. Hydrol.* **2013**, *58*, 253–270. [[CrossRef](#)]
56. Li, Y.F.; Huang, S.Z.; Wang, H.Y.; Zheng, X.D.; Huang, Q.; Deng, M.J.; Peng, J. High-resolution propagation time from meteorological to agricultural drought at multiple levels and spatiotemporal scales. *Agric. Water Manag.* **2022**, *262*, 107428. [[CrossRef](#)]
57. Xu, Y.; Zhang, X.; Wang, X.; Hao, Z.C.; Singh, V.P.; Hao, F.H. Propagation from meteorological drought to hydrological drought under the impact of human activities: A case study in northern China. *J. Hydrol.* **2019**, *579*, 124147. [[CrossRef](#)]
58. Wu, J.W.; Miao, C.Y.; Zheng, H.Y.; Duan, Q.Y.; Lei, X.H.; Li, H. Meteorological and Hydrological Drought on the Loess Plateau, China: Evolutionary Characteristics, Impact, and Propagation. *J. Geophys. Res. Atmos.* **2018**, *123*, 11569–11584. [[CrossRef](#)]
59. He, J.; Yang, K.; Tang, W.J.; Lu, H.; Qin, J.; Chen, Y.Y.; Li, X. The first high-resolution meteorological forcing dataset for land process studies over China. *Sci. Data* **2020**, *7*, 1–11. [[CrossRef](#)]
60. Yang, F.; Lu, H.; Yang, K.; He, J.; Wang, W.; Wright, J.S.; Li, C.W.; Han, M.L.; Li, Y.S. Evaluation of multiple forcing data sets for precipitation and shortwave radiation over major land areas of China. *Hydrol. Earth Syst. Sci.* **2017**, *21*, 5805–5821. [[CrossRef](#)]
61. Han, Y.Z.; Ma, Y.M.; Wang, Z.Y.; Xie, Z.P.; Sun, G.H.; Wang, B.B.; Ma, W.Q.; Su, R.M.Z.; Hu, W.; Fan, Y.X. Variation characteristics of temperature and precipitation on the northern slopes of the Himalaya region from 1979 to 2018. *Atmos. Res.* **2021**, *253*, 105481. [[CrossRef](#)]
62. Shukla, J.; Mintz, Y. Influence of Land-Surface Evapotranspiration on the Earth's Climate. *Science* **1982**, *215*, 1498–1501. [[CrossRef](#)]
63. Zhang, Y.; Kong, D.; Gan, R.; Chiew, F.H.S.; McVicar, T.R.; Zhang, Q.; Yang, Y. Coupled estimation of 500 m and 8-day resolution global evapotranspiration and gross primary production in 2002–2017. *Remote Sens. Environ.* **2019**, *222*, 165–182. [[CrossRef](#)]
64. Zhou, R.S.; Wang, H.L.; Duan, K.; Liu, B.J. Diverse responses of vegetation to hydroclimate across temporal scales in a humid subtropical region. *J. Hydrol.-Reg. Stud.* **2021**, *33*, 100775. [[CrossRef](#)]
65. Elnashar, A.; Zeng, H.W.; Wu, B.F.; Zhang, N.; Tian, F.Y.; Zhang, M.; Zhu, W.W.; Yan, N.N.; Chen, Z.A.; Sun, Z.Y.; et al. Downscaling TRMM Monthly Precipitation Using Google Earth Engine and Google Cloud Computing. *Remote Sens.* **2020**, *12*, 3860. [[CrossRef](#)]
66. Wang, W.; Cui, W.; Wang, X.J.; Chen, X. Evaluation of GLDAS-1 and GLDAS-2 Forcing Data and Noah Model Simulations over China at the Monthly Scale. *J. Hydrometeorol.* **2016**, *17*, 2815–2833. [[CrossRef](#)]
67. Huang, S.; Kumar, R.; Flörke, M.; Yang, T.; Hundecha, Y.; Kraft, P.; Gao, C.; Gelfan, A.; Liersch, S.; Lobanova, A.; et al. Evaluation of an ensemble of regional hydrological models in 12 large-scale river basins worldwide. *Clim. Change* **2017**, *141*, 381–397. [[CrossRef](#)]
68. Tang, L.; Zhao, Z.; Tang, P.; Yang, H. SURE-based optimum-length S-G filter to reconstruct NDVI time series iteratively with outliers removal. *Int. J. Wavelets Multiresolution Inf. Process.* **2019**, *18*, 2050001. [[CrossRef](#)]
69. Arnold, J.G.; Srinivasan, R.; Muttiah, R.S.; Williams, J.R. Large area hydrologic modeling and assessment—Part 1: Model development. *J. Am. Water Resour. Assoc.* **1998**, *34*, 73–89. [[CrossRef](#)]

70. Aloui, S.; Mazzoni, A.; Elomri, A.; Aouissi, J.; Boufekane, A.; Zghibi, A. A review of Soil and Water Assessment Tool (SWAT) studies of Mediterranean catchments: Applications, feasibility, and future directions. *J. Environ. Manag.* **2023**, *326*, 116799. [[CrossRef](#)]
71. Olivera, F.; Valenzuela, M.; Srinivasan, R.; Choi, J.; Cho, H.D.; Koka, S.; Agrawal, A. ArcGIS-SWAT: A geodata model and GIS interface for SWAT. *J. Am. Water Resour. Assoc.* **2006**, *42*, 295–309. [[CrossRef](#)]
72. Awchi, T.A.; Kalyana, M.M. Meteorological drought analysis in northern Iraq using SPI and GIS. *Sustain. Water Resour. Manag.* **2017**, *3*, 451–463. [[CrossRef](#)]
73. Labeledzki, L. Estimation of local drought frequency in central Poland using the standardized precipitation index SPI. *Irrig. Drain.* **2007**, *56*, 67–77. [[CrossRef](#)]
74. Lorenzo-Lacruz, J.; Garcia, C.; Morán-Tejeda, E. Groundwater level responses to precipitation variability in Mediterranean insular aquifers. *J. Hydrol.* **2017**, *552*, 516–531. [[CrossRef](#)]
75. Nalbantis, I.; Tsakiris, G. Assessment of Hydrological Drought Revisited. *Water Resour. Manag.* **2009**, *23*, 881–897. [[CrossRef](#)]
76. Wen, X.; Tu, Y.-H.; Tan, Q.-F.; Li, W.-Y.; Fang, G.-H.; Ding, Z.-Y.; Wang, Z.-N. Construction of 3D drought structures of meteorological drought events and their spatio-temporal evolution characteristics. *J. Hydrol.* **2020**, *590*, 125539. [[CrossRef](#)]
77. Mann, H.B. Nonparametric Tests Against Trend. *Econometrica* **1945**, *13*, 245. [[CrossRef](#)]
78. Zhang, W.; Xi, M.; Liu, H.; Zheng, H. Low sensitivity of net primary productivity to climatic factors in three karst provinces in southwest China from 1981 to 2019. *Ecol. Indic.* **2023**, *153*, 110465. [[CrossRef](#)]
79. Lei, X.; Gao, L.; Wei, J.; Ma, M.; Xu, L.; Fan, H.; Li, X.; Gao, J.; Dang, H.; Chen, X.; et al. Contributions of climate change and human activities to runoff variations in the Poyang Lake Basin of China. *Phys. Chem. Earth Parts A/B/C* **2021**, *123*, 103019. [[CrossRef](#)]
80. Parzen, E. On Estimation of a Probability Density Function and Mode. *Ann. Math. Stat.* **1962**, *33*, 1065–1076. [[CrossRef](#)]
81. Zhang, Z.X.; Feng, Z.Q.; Zhang, H.Y.; Zhao, J.J.; Yu, S.; Du, W. Spatial distribution of grassland fires at the regional scale based on the MODIS active fire products. *Int. J. Wildland Fire* **2017**, *26*, 209–218. [[CrossRef](#)]
82. Tan, S.K.; Hu, B.X.; Kuang, B.; Zhou, M. Regional differences and dynamic evolution of urban land green use efficiency within the Yangtze River Delta, China. *Land Use Policy* **2021**, *106*, 105449. [[CrossRef](#)]
83. Hudgins, L.; Friehe, C.A.; Mayer, M.E. Wavelet transforms and atmospheric-turbulence. *Phys. Rev. Lett.* **1993**, *71*, 3279–3282. [[CrossRef](#)]
84. Hauke, J.; Kossowski, T. Comparison of Values of Pearson’s and Spearman’s Correlation Coefficients on the Same Sets of Data. *Quaest. Geogr.* **2011**, *30*, 87–93. [[CrossRef](#)]
85. Torrence, C.; Compo, G.P. A Practical Guide to Wavelet Analysis. *Bull. Am. Meteorol. Soc.* **1998**, *79*, 61–78. [[CrossRef](#)]
86. Grinsted, A.; Moore, J.C.; Jevrejeva, S. Application of the cross wavelet transform and wavelet coherence to geophysical time series. *Nonlinear Process. Geophys.* **2004**, *11*, 561–566. [[CrossRef](#)]
87. Zhang, Y.; You, Q.; Lin, H.; Chen, C. Analysis of dry/wet conditions in the Gan River Basin, China, and their association with large-scale atmospheric circulation. *Glob. Planet. Change* **2015**, *133*, 309–317. [[CrossRef](#)]
88. Zhou, H.; Liu, Y.B. SPI Based Meteorological Drought Assessment over a Humid Basin: Effects of Processing Schemes. *Water* **2016**, *8*, 373. [[CrossRef](#)]
89. Zhang, D.; Chen, P.; Zhang, Q.; Li, X. Copula-based probability of concurrent hydrological drought in the Poyang lake-catchment-river system (China) from 1960 to 2013. *J. Hydrol.* **2017**, *553*, 773–784. [[CrossRef](#)]
90. Brouziyne, Y.; Abouabdillah, A.; Chehbouni, A.; Hanich, L.; Bergaoui, K.; McDonnell, R.; Benaabidate, L. Assessing Hydrological Vulnerability to Future Droughts in a Mediterranean Watershed: Combined Indices-Based and Distributed Modeling Approaches. *Water* **2020**, *12*, 2333. [[CrossRef](#)]
91. Zhang, S.; Wu, Y.; Sivakumar, B.; Mu, X.; Zhao, F.; Sun, P.; Sun, Y.; Qiu, L.; Chen, J.; Meng, X.; et al. Climate change-induced drought evolution over the past 50 years in the southern Chinese Loess Plateau. *Environ. Model. Softw.* **2019**, *122*, 104519. [[CrossRef](#)]
92. Kang, H.; Sridhar, V. Combined statistical and spatially distributed hydrological model for evaluating future drought indices in Virginia. *J. Hydrol. Reg. Stud.* **2017**, *12*, 253–272. [[CrossRef](#)]
93. Hong, X.; Guo, S.; Chen, G.; Guo, N.; Jiang, C. A Modified Two-Parameter Monthly Water Balance Model for Runoff Simulation to Assess Hydrological Drought. *Water* **2022**, *14*, 3715. [[CrossRef](#)]
94. Liu, Y.; Shan, F.; Yue, H.; Wang, X.; Fan, Y. Global analysis of the correlation and propagation among meteorological, agricultural, surface water, and groundwater droughts. *J. Environ. Manag.* **2023**, *333*, 117460. [[CrossRef](#)] [[PubMed](#)]
95. Guo, H.; Bao, A.; Ndayisaba, F.; Liu, T.; Jiapaer, G.; El-Tantawi, A.M.; De Maeyer, P. Space-time characterization of drought events and their impacts on vegetation in Central Asia. *J. Hydrol.* **2018**, *564*, 1165–1178. [[CrossRef](#)]

Disclaimer/Publisher’s Note: The statements, opinions and data contained in all publications are solely those of the individual author(s) and contributor(s) and not of MDPI and/or the editor(s). MDPI and/or the editor(s) disclaim responsibility for any injury to people or property resulting from any ideas, methods, instructions or products referred to in the content.